

Mechanical characterization and modeling of the deformation and failure of the highly crosslinked RTM6 epoxy resin

X.P. Morelle¹ · J. Chevalier¹ · C. Bailly² · T. Pardoen¹ · F. Lani¹

Received: 13 May 2016 / Accepted: 19 December 2016
© Springer Science+Business Media Dordrecht 2017

Abstract The nonlinear deformation and fracture of RTM6 epoxy resin is characterized as a function of strain rate and temperature under various loading conditions involving uniaxial tension, notched tension, uniaxial compression, torsion, and shear. The parameters of the hardening law depend on the strain-rate and temperature. The pressure-dependency and hardening law, as well as four different phenomenological failure criteria, are identified using a subset of the experimental results. Detailed fractography analysis provides insight into the competition between shear yielding and maximum principal stress driven brittle failure. The constitutive model and a stress-triaxiality dependent effective plastic strain based failure criterion are readily introduced in the standard version of Abaqus, without the need for coding user subroutines, and can thus be directly used as an input in multi-scale modeling of fibre-reinforced composite material. The model is successfully validated against data not used for the identification and through the full simulation of the crack propagation process in the V-notched beam shear test.

Keywords RTM6 · Highly crosslinked epoxy resin · Elasto-viscoplasticity · Fracture criterion · Constitutive modeling · Aerospace composite

1 Introduction

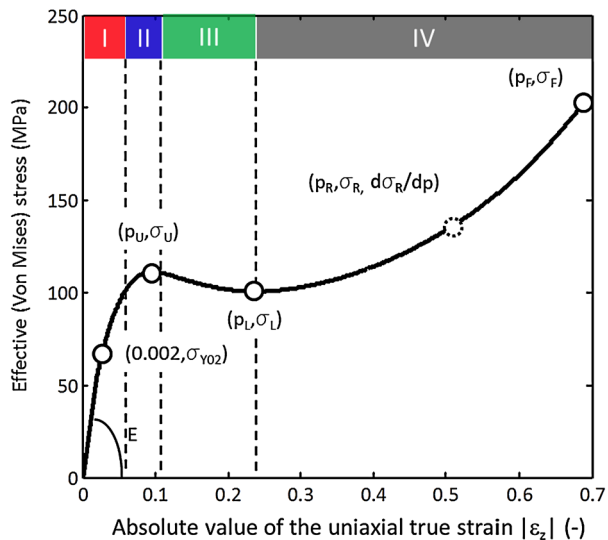
Multi-scale mechanical modeling frameworks require reliable constitutive models and failure criteria for the constituents as well as accurate experimental data for parameter identification in order to reach the highest possible predictive capability for stress analysis, in the context of virtual testing of complex composite systems, or for the purpose of designing new hybrid materials (LLorca et al. 2011; Canal et al. 2012). High performance adhesives

✉ X.P. Morelle
morelle.xavier@gmail.com

¹ Institute of Mechanics, Materials and Civil Engineering, Université catholique de Louvain, Place Sainte-Barbe, No. 2, L5.02.02, 1348 Louvain-la-Neuve, Belgium

² Institute of Condensed Matter and Nanosciences, Université catholique de Louvain, Croix du Sud, No. 1, L7.04.02, 1348 Louvain-la-Neuve, Belgium

Fig. 1 The four deformations stages of an amorphous glassy polymer: stage I—elastic-viscoelastic deformation; stage II—onset of plastic flow; stage III—strain softening; stage IV—strain-hardening. The illustrative curve is taken from a room temperature compression test on RTM6, with effective (von Mises) stress plotted against the absolute value of the uniaxial true compression strain $|\epsilon_z|$



and polymer composites constitute two important families of hybrid systems, among which many rely on thermoset epoxy resins. Two main classes of epoxies have been studied in the literature, from both mechanical characterization and modeling standpoints:

- The largest part of the literature focuses on moderately crosslinked ductile epoxies, based on a difunctional precursor such as diglycidyl ether of bisphenol A or DGEBA and tetrafunctional, mostly amine, hardener. They are typically blended with other constituents and used for structural adhesive applications. These systems can be quite tough and ductile.
- A more limited part of the literature is dedicated to the characterization and modeling of the deformation and failure behavior of highly crosslinked epoxies such as RTM6, which are based on tetrafunctional precursor and (amine) hardener. These systems are usually quite brittle.

The stress-strain response of these epoxies is similar to that of amorphous glassy thermoplastics. Depending on the loading conditions (strain rate, temperature, stress triaxiality), amorphous glassy polymers including highly crosslinked epoxies can exhibit four different deformation stages, as illustrated in Fig. 1 (in this figure, the reference data used in this work for model identification are highlighted by circles).

First, the response is elastic-viscoelastic (stage I), where the deformation is due to secondary interactions (Meijer and Govaert 2005; G'Sell and Jonas 1981). As the viscoelastic component increases with time, the curve slowly departs from linearity, due to limited retarded molecular movements. This small strain region can be significantly affected by the strain-rate and temperature because of the viscoelastic component.

Second, the yield process starts and plastic flow sets in (stage II), as the activation barrier to main chain segmental motion is overcome. The yield transient is very much affected by the strain-rate, temperature, and hydrostatic pressure; see, e.g., Eyring's theory (Eyring 1936; Ree and Eyring 1955) of transition of state, or Argon's thermomechanically activated double-kink mechanism (Argon 1973; Argon and Bessonov 1977), as well as by the thermomechanical history of the polymer, related to physical aging (increase) or mechanical rejuvenation (decrease) (Meijer and Govaert 2005; Tervoort et al. 1996; Klompen et al. 2005; Govaert et al. 2000).

Third, and closely following the yield point, softening occurs due to large collective molecular movement (stage III). The origin of softening is still subject to debate. When strain-localization/necking is enabled due to the specimen geometry and boundary conditions, softening can obviously occur through the development of macroscopic shear bands. If the rehardening capability is sufficient to delocalize the deformation, the shear bands thicken and the sample rehardens as a whole. If rehardening does not take place, the specimen fails (Melick et al. 2003a; Wu and van der Giessen 1995). In other circumstances, in the case no shear banding is extrinsically triggered, it is now admitted that micro-shear banding can occur as a true material feature. The kinetics of initiation, growth, and coalescence of shearing zones determine the yield drop and softening rate (Sindt et al. 1996; Hasan and Boyce 1995; Homer and Schuh 2009; Quinson et al. 1996; Oleynik 1989). Both the onset of yielding and the softening stage are believed to be associated with free-volume rearrangement (Struik 1991; Hasan et al. 1993; Jatin et al. 2013).

Finally, it is generally admitted that a “rubberlike” nonlinear response of the network starts to prevail at large strains through chain reorientation (Sindt et al. 1996; G’Sell and Gopez 1985) balanced by the fact that only limited stretch ratios can be achieved in highly crosslinked thermosets. This phenomenon is called strain rehardening (stage IV) and can be interpreted as being analogous to the entropic resistance to the alignment of the molecular network. The response is commonly considered to be independent of prior thermomechanical history but can be much affected by the cross-links density (Melick et al. 2003b; Seden et al. 2010) and, to a lesser extent, by temperature and rate (Govaert et al. 2008). Final failure occurs when segments of the molecular chains are statistically stressed above some critical chain scission stress (Andrews and Reed 1978).

This behavior has been largely reported for thermoplastic polymers (e.g., PMMA and PC) loaded in compression, shear, or tension up to very large fracture strains. Hence, there is ample literature on the joint thermomechanical characterization and finite strain elastic-viscoplastic constitutive modeling of the strain-rate, temperature, and pressure sensitive response of glassy polymers up to very large deformations (Haward and Thackray 1968; Boyce et al. 1988; Tervoort and Govaert 1998; Klompen and Govaert 1999; Marano and Rink 2008).

Large fracture strains are also attained in moderately and highly crosslinked epoxies loaded in uniaxial compression. Unlike RTM6 which usually fails before the softening stage for any other loading than compression, moderately crosslinked epoxies can still exhibit some ductility (i.e., chain mobility) in shear and tension. The macroscopic response of RTM6 loaded in compression exhibits many similarities with glassy thermoplastics loaded in tension or compression, which suggest that the fundamental origins of plastic flow, softening, and rehardening are identical in both types of polymers (Yamini and Young 1980). However, no similarity in terms of progressive damage mechanisms (e.g., crazing) has ever been reported (Asp et al. 1996). In summary, although RTM6 and other thermoset epoxy resins exhibit a hardening response and pressure dependence of yielding similar to amorphous glassy thermoplastics, their failure is more sensitive to the stress triaxiality as a result of a reduced mobility of the network and of the presence of microscopic defects which act as stress concentrators (Chevalier et al. 2016).

Most research dealing with the characterization and modeling of thermoset epoxy resins covers only a part of the triangle “strain-rate—temperature—pressure” sensitivity of the relationship between stress and strain. Besides, some works are dealing only with the characterization of the strain-rate, temperature, and pressure dependence of the peak yield (e.g., Gómez-del Río and Rodríguez (2012), Sindt et al. (1996), Gerlach et al. (2008)), while others cover the full range of deformation, including softening and rehardening when these

stages are actually observed (Poulain et al. 2013, 2014). Moreover, most studies focusing on the nonlinear behavior of the resin do not address the problem of final failure, and vice versa. An interesting common point to several studies is the characterization and modeling of the competition between shear yielding related to fundamental intrinsic shear deformation mechanisms (Bowden and Raha 1974; Sindt et al. 1996; Hasan and Boyce 1995), and micro-cavitation occurring mainly in the presence of positive hydrostatic stress and/or positive maximum principal stress (Liang and Liechti 1996; Asp et al. 1996; Fiedler et al. 2001, 2005; Hobbiebrunken and Fiedler 2007).

Very few studies have been dedicated to the detailed modeling of the deformation and failure of the structural RTM6 epoxy resin itself. It is worth mentioning the work by Gerlach et al. (2008) in which the RTM6 was tested at room temperature both in compression and tension under impact loading, covering about six decades of strain rates. Their results showed the linear dependence of the peak-yield stress on the natural logarithm of the strain rate, with a slope transition between *quasi-static* and *impact* regimes. The experimental results revealed also a strong dependence of the apparent Young's modulus on the strain rate, with again a transition between *quasi-static* and *impact* regimes. This strong rate dependent behavior of RTM6 was modeled up to the peak yield using the Goldberg elastic–viscoplastic model (Goldberg et al. 2003), also accounting for effects of the hydrostatic pressure. In (Hobbiebrunken et al. 2005), the RTM6 epoxy resin was characterized in uniaxial tension at different temperatures and a single low strain-rate. A strong dependence of the yield stress, failure stress, and failure strain on temperature was found. Shear yielding was observed at high temperatures while a brittle behavior dominated at lower temperatures. A von Mises yield surface and associated flow rule were used, with simple rate independent hardening law fitted to the experimental curves at the different temperatures. One of the salient facts of their study was the strong effect of the resin nonlinear stress–strain response on the resulting composite thermal residual stress.

There is a growing demand for better mechanical characterization of structural epoxies coming from experts in modeling as well as from materials designers and engineers dealing with the stress analysis of composites. Therefore, a large characterization and modeling effort has been carried out in this work on the highly crosslinked RTM6 structural epoxy resin commercialized by Hexcel corp. The first aim of this research is to attain a better understanding of the competition between thermally and stress activated shear-dominated (visco-)plastic deformation as well as micro-cavitation–induced brittle failure. The second expected outcome of this study is to provide the community with a carefully assessed empirical strain-rate, temperature, and pressure sensitive constitutive model and a pressure-dependent failure criterion (the latter at room temperature only) for the RTM6 epoxy resin involving the corresponding set of identified parameters. The models are ready for use “as is” in most commercial general purpose finite element software, and in particular with Abaqus (V6.12 2016). The proposed constitutive model can be seen as a degraded version of more complex finite strain elastic–viscoplastic constitutive models developed and identified, for instance, by Poulain et al. (2014) on epoxy, Boyce et al. (1988), Tervoort and Govaert (1998), Anand and Gurtin (2003), Anand et al. (2009), Ames et al. (2009), Srivastava et al. (2010) on PC or PMMA. Nevertheless, while keeping most of the essential characteristics of those models (with the exception of possible kinematic hardening components), it has the user-friendly advantage for engineers and researchers of avoiding the need for user material subroutines. This paper addresses monotonic loading along radial or near radial paths and does not address the aspects of relaxation and creep (Morelle et al. 2014; Morelle 2015) or the response of the system upon load reversal and other back stress issues (Marano and Rink 2006; Westbrook et al. 2011; Morelle 2015).

The paper is organized as follows: Sect. 2 presents the materials and manufacturing conditions of the test samples. Section 3 describes all the mechanical tests. Section 4 presents the experimental results (compression, tension, torsion) that will be used for the identification and preliminary assessment of the constitutive model, as well as a detailed fracture analysis after the different mechanical tests. Section 5 explains the formulation of the nonlinear constitutive model, its identification against experimental results and validation. Section 6 presents a selection of failure criteria, their identification and validation. Section 7 contains the first critical full assessment of the deformation and failure model by comparison of FE simulation results and experimental data for the V-notch beam (Iosipescu) test. Final conclusions and perspectives are described in Sect. 8.

2 Materials

Hexflow RTM6, supplied by Hexcel, is a mono-component epoxy resin specifically developed to fulfill the requirements of the aeronautics and space industry regarding advanced resin transfer moulding processes. This highly-crosslinked thermoset is obtained from a premixed epoxy system, composed of a tetra-functional epoxide precursor (tetra-glycidyl methylene dianiline or TGMDA) and a blend of two di-amine hardeners (MDEA and MMIPA) (Kiuna et al. 2002; Dumont 2013). RTM6 shows good processability through a convenient injection window for industrial use.

After curing, RTM6 has a glass transition temperature (T_g) around 220°C, determined by differential scanning calorimetry (DSC) and dynamic mechanical analysis (DMA) testing, providing high stiffness ($E = 3$ GPa at room temperature) and good thermal stability properties with a service temperature ranging from -60°C to 180°C.

A specific cure cycle was developed in order to manufacture thick resin slabs and cylinders with a minimum of 95 % degree of conversion while avoiding resin degradation in the core of the specimen. Hence, a large variety of test specimens were manufactured with reproducible thermomechanical history and consistent thermomechanical properties. The uncured resin mixture was first poured in open release-agent coated molds and degassed for 75 min at 90°C under vacuum. Then, in an air-circulated oven, the applied curing cycle used a 2°C/min heating ramp to 130°C, 3 h dwell at 130°C, 2°C/min heating to 180°C, and finally 3 h of post-curing at 180°C to achieve the expected degree of conversion. The reproducibility of the materials microstructure after curing was verified at several locations of specimens obtained in the different molds by measuring the residual reaction enthalpy with modulated DSC, confirming that the degree of cure was consistently between 95 % and 97 %.

3 Mechanical testing procedures

3.1 Specimen geometries

Cylindrical resin slabs were machined into small cylindrical specimens for uniaxial compression tests and into cylindrical dog-bone specimens for the uniaxial tensile tests. Notched tensile specimens were prepared by machining the cylindrical dog-bone specimen with different notch radii. Larger cylindrical slabs were produced in order to machine hollow torsion specimen. V-notched beam specimens were obtained from rectangular slabs. The different specimens are shown in Fig. 2, the dimensions and standards that have been followed are provided in Table 1.

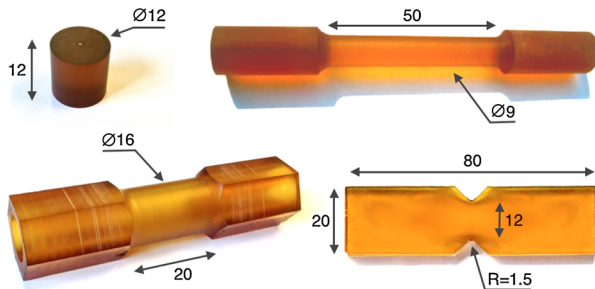


Fig. 2 Bulk resin samples for mechanical testing. (*Top-left*) Cylindrical samples for uniaxial compression testing; (*top-right*) dog-bone specimen for uniaxial tension (note that notched specimens were also manufactured); (*bottom-left*) hollow tubular sample for torsion testing; (*bottom-right*) V-notch beam specimen for model assessment. Main dimensions are indicated in millimeters, for the complete detail please refer to Table 1

Table 1 Summary of dimensions and corresponding inspirational standards for all tested specimens

Type of test	International standard	Length (mm)	Diameter (mm)	Notch radius (mm)
Uniaxial compression	ASTM D695	12	12	–
Uniaxial compression testing sensitivity to friction	ISO604	6	12	–
Uniaxial tension (Small specimen)	ASTM D638	36 (gauge length)	6	–
Uniaxial tension (Large specimen)	ASTM D638	50 (gauge length)	9	–
Notched tension	–	50 (gauge length)	9 (original diameter) and 4 (section diameter in the notch)	1, 3, 5
Torsion	–	20 (gauge length)	16 (outer diameter) and 12 (inner diameter)	–
Iosipescu	ASTM D5379	80 (length) and 20 (height)	4 (thickness)	V-notch of 90° opening angle with end-radius of 1.5

3.2 Test methods

The compression, tension, notched tension, and V-notch beam tests were carried out on a screw-driven universal testing machine (Zwick-Roell with an external load cell of 250 kN). The torsion tests were performed on a hydraulic axial-torsion machine MTS (model 809 axial/torsional) with a 250 kN load cell and a 2200 N/m torque cell capacity. The tests were performed in a conditioned room with controlled temperature ($23 \pm 3^\circ\text{C}$) and relative humidity ($50 \pm 10\%$). The target temperature and relative humidity are selected according to ASTM D3479.

The compression tests were performed either at a constant true compressive strain rate (CSR) with $\frac{|de_z|}{dt}$ varying between 10^{-4} and 0.1 s^{-1} by using a closed-loop crosshead dis-

placement control method or at constant crosshead displacement rate (CDR) corresponding to compressive strain rates $\frac{|de_2|}{dt}$ between $2.32 \cdot 10^{-4}$ and 0.26 s^{-1} . Teflon strips were used as solid lubricant between the compression platens and the samples in order to minimize the barreling effect. Compared with any other liquid lubricant (e.g., grease oil), Teflon was most effective at minimizing specimen barreling. All the compression tests were performed at three different temperatures: room temperature $\approx 20^\circ\text{C}$ (293 K), 100°C (373 K), and 150°C (423 K). The axial strain was obtained from the crosshead displacement, corrected in order to account for the machine compliance. The absence of friction and shear-banding or localization allows using experimental results for the construction of reliable effective stress/effective strain curves. At room temperature, on a subset of compression samples, the radial strain was measured either by using an LVDT or by analyzing images taken from videos of the tests, allowing for the estimation of the plastic Poisson ratio. The measurement of the plastic Poisson ratio at higher temperatures was not possible as both the LVDT and camera are not compatible with the configuration of our climatic chamber.

The behavior in tension has been characterized either at a constant true strain rate of 10^{-3} s^{-1} (CSR tests) using a closed-loop crosshead displacement control method, or at a constant crosshead displacement rate of 1 mm/min (CCDR tests). The CSR tests were performed at room temperature only, while the CCDR tests were performed at room temperature $\approx 20^\circ\text{C}$ (293 K), 100°C (373 K), and 150°C (423 K). The axial strain was measured using contact extensometers in the gauge length. Above 100°C , localization occurred in a subset of specimen. The option taken was to exclude these specimens out of the database for the identification of the constitutive model.

The response of the notched tensile specimens, with three different radii, has been determined at a CCDR of 1 mm/min, at room temperature only. The radial displacement in the notch was measured using a strictometer (LVDT).

The torsion tests were conducted at room temperature and under a single rotation rate of $7^\circ/\text{min}$. Three-element 45° rectangular rosette strain gauges were bonded onto the torsion specimen outer surface to measure the shear strain in the gauge section. Such strain gauges cannot operate above 10–15 % of strain; therefore, a correlation was used between the measured value of shear strain (with the strain gauge) and the applied rotation angle in order to get a reliable estimate of larger shear strain. The large majority of the tests failed before shear-localization could be observed, making these tests eligible for the identification of the parameters of a constitutive model. The heterogeneity of stress along the radial direction in the cylinder wall was neglected in the identification procedure of the shear-stress/shear-strain relationship. The validity of the assumption was verified by nonlinear three-dimensional finite element simulations of the full torsion test, in which both the strain-gauge measurement and the crosshead rotation/couple, as well as the occurrence of failure before the onset of localization on the outer surface of the specimen, could be reproduced.

The V-notched beam tests were conducted at room temperature only, with a single crosshead displacement rate of 1 mm/min. Back-to-back bidirectional strain gauges were bonded onto the specimen surface between the notch roots at 45° with respect to the horizontal axis, in order to measure the local maximum and minimum principal strains, translated into shear strain.

A minimum of three valid test results are available for each condition, except for the CCDR compression tests, where, besides the 1 mm/min case where six valid tests results are available, only one or two samples could be tested. The CSR tests were performed with a single batch of resin. Samples taken from several batches were used to conduct the other tests. Note that, within the same batch, limited variability of the elastic and yield behavior is observed, whereas the failure stress and strain can show an important scatter. Significant

batch-to-batch variability can be observed for most of the measured mechanical properties. Nevertheless, the obtained results remain eligible for further analysis.

3.3 Note on the determination of a representative strain rate

None of the CSR or the CCDR test conditions lead to a constant effective plastic strain rate over the entire deformation range. However, when assessing the nonlinear deformation behavior of materials, a comparison between hardening curves is meaningful only when similar effective plastic strain evolutions are produced in the different tests, e.g., Liang and Liechti (1996) invoke differences of strain-rate between different tests to explain certain inconsistencies of hierarchy of yield strengths between different types of tests.

Starting from the definition of the plastic strain tensor p_{ij}

$$p_{ij} = \varepsilon_{ij} - S_{ijkl}\sigma_{kl} \quad (1)$$

where ε_{ij} is the true (logarithmic or Hencky) strain tensor derived from the experiments, S_{ijkl} is the material's compliance tensor, and σ_{kl} is the experimental true stress tensor, the plastic strain rate tensor is computed through the following approximation (for discretely sampled data)

$$\frac{dp_{ij}}{dt} = \frac{p_{ij}^{t+\Delta t} - p_{ij}^t}{\Delta t}. \quad (2)$$

The effective plastic strain rate is defined as

$$\frac{dp}{dt} = \sqrt{\frac{2}{3} \frac{dp_{ij}}{dt} \frac{dp_{ij}}{dt}}. \quad (3)$$

The average effective plastic strain rate computed over the strain range $[0, p_f]$, is given by

$$\left\langle \frac{dp}{dt} \right\rangle_{p \leq p_f} = \sqrt{\frac{2}{3} \left\langle \frac{dp_{ij}}{dt} \right\rangle \left\langle \frac{dp_{ij}}{dt} \right\rangle} \quad (4)$$

with

$$\left\langle \frac{dp_{ij}}{dt} \right\rangle = \frac{p_{ij}|_{t_f}}{t_f}. \quad (5)$$

For a uniaxial test along the z -axis, assuming plastic incompressibility, the average effective plastic strain rate is given by $\langle \frac{dp}{dt} \rangle = \langle |\frac{dp_z}{dt}| \rangle$ with $p_z = \varepsilon_z - \frac{\sigma_z}{E}$, where E is the Young's modulus measured in tension or compression.

Two measures of the time-average effective plastic strain rate are used, which allow a comparison of the strain-rate sensitivity of the materials: a “*low-range*” or small strain average ($p \leq 0.07$) and a “*full-range*” or large strain average ($p \leq 0.7$). When early failure of the specimen is observed before the effective plastic strain has reached 0.07, the plastic strain evolution is extrapolated up to 0.07 in such a way as to mimic the response of a compression or torsion test, providing an estimate of the low-range effective plastic strain rate average. Besides, thorough examination of the compression tests shows that the full-range average is about 3/2 of the low-range average, providing also an estimate of the full-range average effective plastic strain rate for specimens that do not exhibit large ductility.

Here is a summary of how these effective plastic strain rate averages are used:

- When comparing compression tests only, the “*full-range*” effective plastic strain rate average is available and used;

- When comparing tensile tests only, the “*low-range*” effective plastic strain rate average is used, either based on the available data or estimated by extrapolation up to 0.07;
- When comparing different types of tests, the full-range effective plastic strain rate average is used, either based on available data (for compression tests) or on estimations by extrapolation.

4 Experimental results

4.1 Mechanical test results

The mechanical response of RTM6 will be mainly presented under the form of “effective stress–effective plastic strain” curves. These curves are carefully analyzed in terms of the reference features and/or data points as illustrated in Fig. 1:

- The elastic modulus, E ;
- The stress at a 0.002 effective plastic strain, $\sigma_{0.002}$;
- The peak stress, σ_U , and effective plastic strain at peak stress, p_U ;
- The lower stress, σ_L ;
- The failure stress, σ_F , and effective plastic strain at failure, p_F .

The other data such as the effective plastic strain p_L at the lower yield level σ_L or the incremental strain-hardening coefficient $\frac{d\sigma}{dp}$ at an intermediate effective plastic strain p_R in the rehardening process will not be addressed in details although they can be used in the identification of the hardening law.

The variation of the elastic modulus in compression as a function of strain rate is shown in Fig. 3(a) for various temperatures. The temperature dependence of the elastic modulus in tension is shown in Fig. 3(b). Note that the compressive and tensile CSR tests were made with the same batch while the CCDR compressive and tensile tests were performed with samples coming from different batches, but without samples coming from the “CSR batch.” As a result, the batch to batch variability of the modulus is from 10 to 15 %, whatever the temperature. The static moduli are in good agreement with the Young’s modulus measured

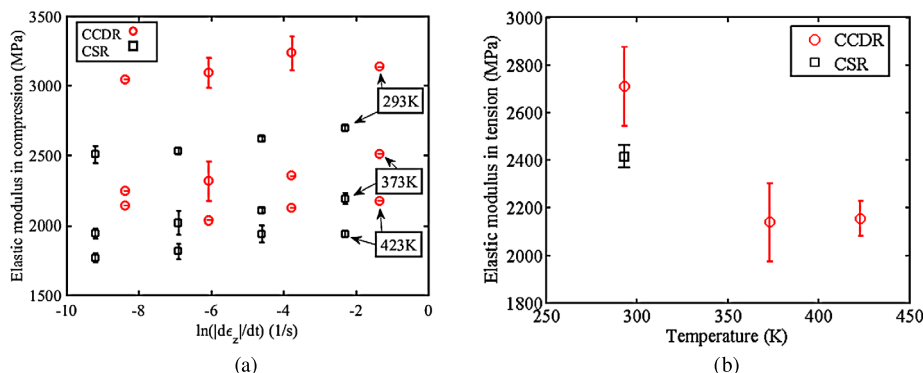


Fig. 3 Measured temperature and strain-rate dependence of the Young’s modulus in (a) compression with Constant Strain Rate (CSR—black squares) tests on a single batch, and with Constant Crosshead Displacement Rate (CCDR—red circles) tests on multiple batches, (b) under tension with both CSR (single-batch) and CCDR (multi-batch) test conditions (Color figure online)

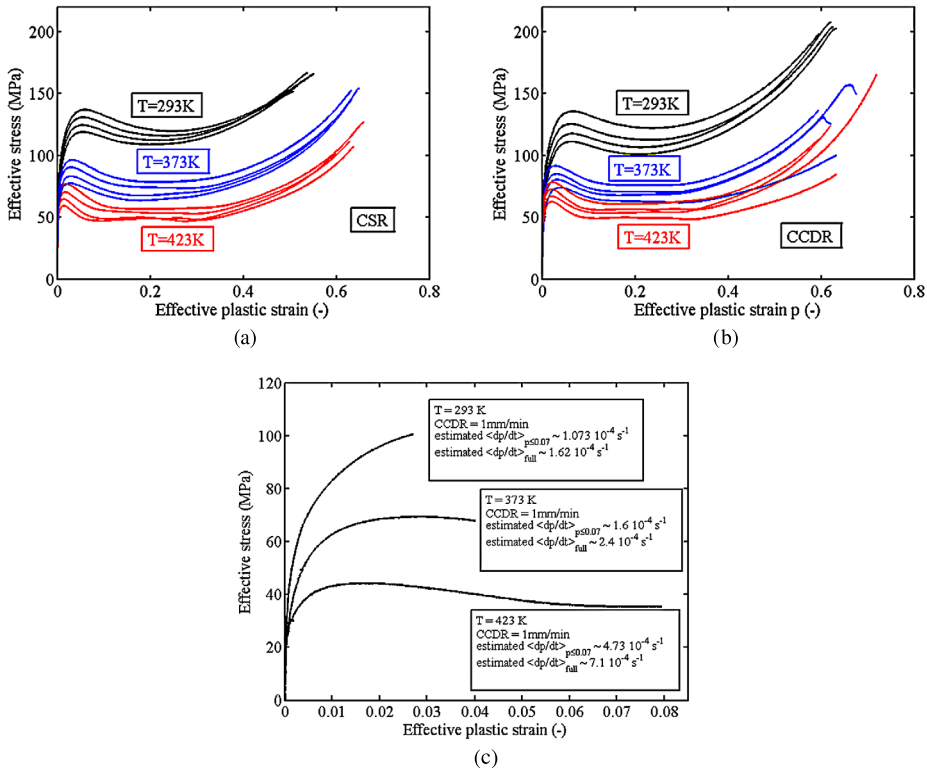


Fig. 4 Representative effective stress versus effective plastic strain curves for three temperatures (293, 373, and 423 K) in (a) compression with CSR tests (from 10^{-4} to 10^{-1} s^{-1}) and a single batch, (b) compression with CCDR (from 0.1 to 100 mm/min) and multiple batches, (c) tension with CCDR (the estimated average effective plastic strain rates are also provided). Note that tensile tests conducted at CSR were partially invalidated due to sliding in the grips and are not shown (only the elastic modulus and corrected final failure stress were kept in the database)

by dynamic mechanical analysis (Morelle 2015), although not all the batches were analyzed with this technique.

Compression tests results at CSR and CCDR are shown in Fig. 4(a) and (b), respectively. Tensile test results at CCDR are shown in Fig. 4(c). A single effective stress–effective plastic strain curve per condition is shown in these figures (these curves were selected as good average representative of the stress–strain behavior). The tensile curves obtained at CSR are not shown as sliding within the grips was observed; although the tests had to be invalidated, the measured elastic moduli and corrected failure stress were consistent and thus kept in the database. Note that when plotting the effective stress as a function of the effective plastic strain, nonzero stresses at zero plastic strain are usually observed, at a value close to $\sigma_{0.002}$. In Fig. 4(c), the low and full-range averages of the effective plastic strain rate are shown for information. A comparison of Fig. 4(a) and (b) reveals that there is a 50 MPa stress decrease and a 0.1 plastic strain decrease at failure for the CSR tests conducted at room temperature. No other explanation than the batch/operator variability can be given to explain this difference. The Poisson ratio and the plastic Poisson ratio were measured on a subset of uniaxial compression tests, giving average values equal to ≈ 0.34 and ≈ 0.5 (minimum

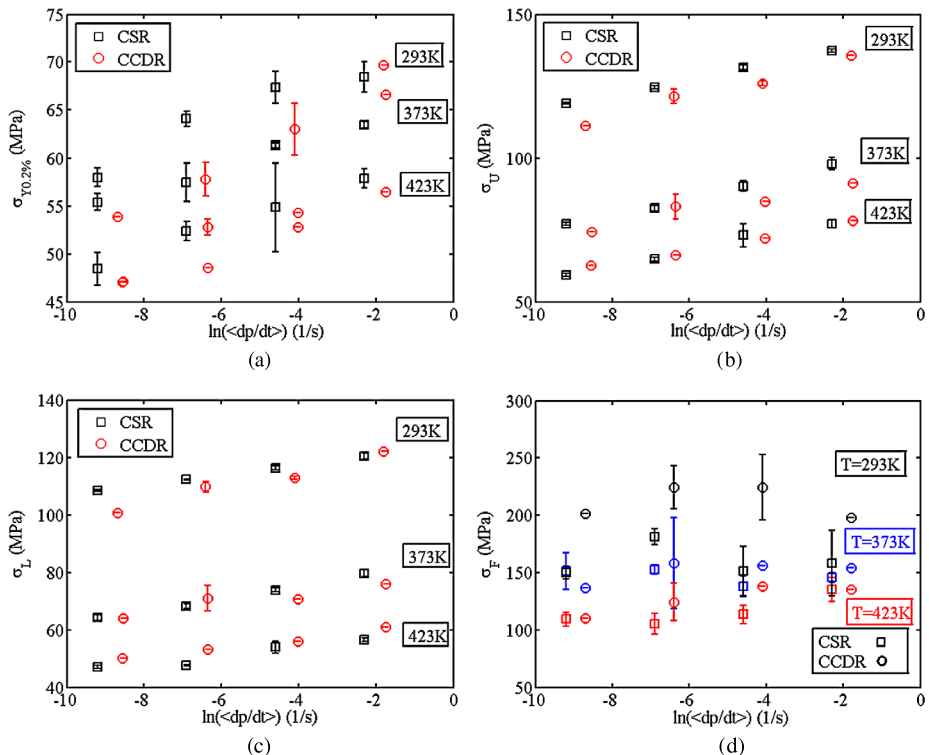


Fig. 5 Strain-rate dependence of the reference effective stress values for uniaxial compression tests (defined in Fig. 1): (a) stress at 0.002 effective plastic strain $\sigma_{0.002}$, (b) peak stress σ_U , (c) lower stress σ_L , and (d) failure stress σ_F . The abscissa in the graphs is the full-range average effective plastic strain rate

value, 0.48; maximum, 0.51), respectively. The latter suggests that plastic deformation is isochoric.

Figure 5 illustrates the strain-rate and temperature dependence of the reference effective stress values $\sigma_{0.002}$, σ_U , σ_L , and σ_F defined in Fig. 1 for uniaxial compression tests. Batch-to-batch variability of up to 10 % can be observed for the stress at 0.002 effective plastic strain, the peak and the lower stresses, whatever the strain-rate and temperature. In Fig. 5(a)–(c), the stress varies linearly with the natural logarithm of the average effective plastic strain rate. The range of strain-rates addressed in this paper does not allow capturing the transition from quasi-static to impact regimes such as observed by Gerlach et al. (2008). Figure 5(d) suggests that the failure stress in compression is almost insensitive to the plastic strain rate, and also shows a large variability, in general.

To complement the analysis of the strain-rate and temperature dependence of the mechanical response in uniaxial compression, Fig. 6(a) and (b) also show the evolution of the effective plastic strain at peak stress p_U and effective plastic strain at failure p_F , respectively. Both are rather insensitive to strain-rate, and, when considering the CSR tensile tests at room temperature as outliers, the plastic strain at failure is almost independent of temperature.

A comparison of representative effective stress–effective plastic strain curves determined based on the compression, tension and torsion tests is shown in Fig. 7, where the estimated average effective plastic strain rates $\langle \frac{dp}{dt} \rangle$ are also indicated. In this figure, the effect of an

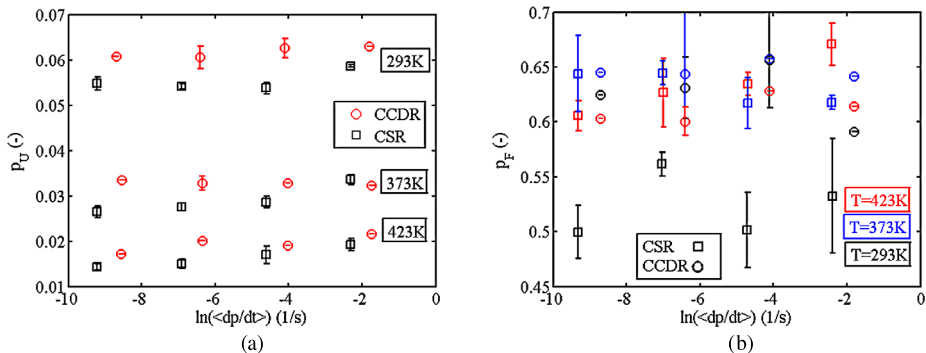


Fig. 6 Strain-rate dependence of the reference effective plastic strain values for uniaxial compression tests (defined in Fig. 1): (a) effective plastic strain at peak stress p_U and (b) effective plastic strain at failure p_F . The abscissa in the graphs is the full-range average effective plastic strain rate

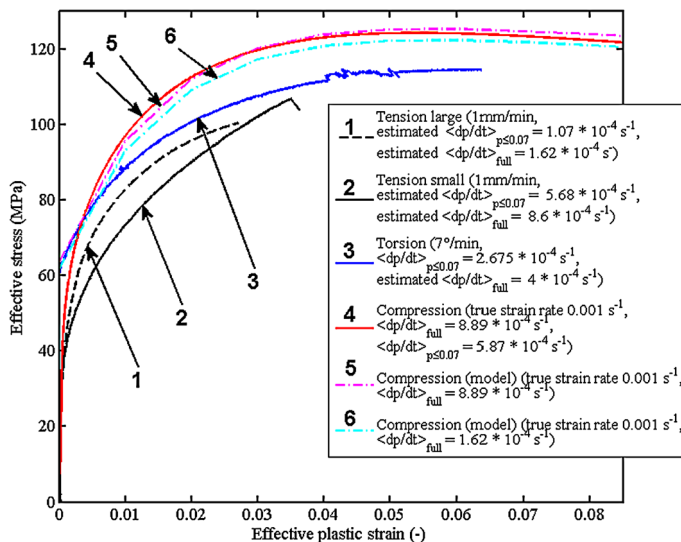


Fig. 7 Representative “Effective (von Mises) stress versus effective plastic strain curve” for the different types of loadings (compression, tension, torsion). Also shown: estimates of the “low-range” and “full-range” average effective plastic strain rates

error in the estimation of the average effective plastic strain rate on the stress–strain curve is shown, anticipating the use of the constitutive model presented in the next sections. In particular, it highlights the fact that a correct estimation of the average effective plastic strain rate is important when attempting the identification of the asymmetry of yielding between tension and compression.

Finally, the pressure and temperature dependence of the effective (von Mises) stress σ_e and effective plastic strain at failure p_F are shown in Fig. 8(a) and (b). In these figures, the x -axis corresponds to the stress triaxiality defined as

$$\text{Stress triaxiality} = \frac{\sigma_{mm}}{3\sigma_e} \quad (6)$$

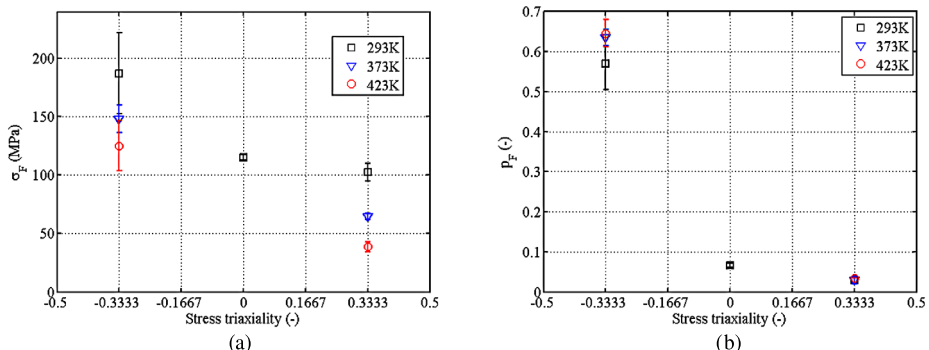


Fig. 8 (a) Variation of the effective failure stress as a function of stress triaxiality (tension = 1/3, torsion = 0, compression = -1/3) and (b) variation of the effective plastic strain at failure as a function of stress triaxiality

where $\frac{\sigma_{mm}}{3}$ is the hydrostatic stress. The plotted stress and plastic strain values are actually averaged over all the strain-rates.

4.2 Fractographic analysis

The tensile and notched tensile specimens failed in a brittle manner after limited plastic deformation, with very similar fracture surfaces. Figure 9(a) shows SEM micrographs, and Fig. 9(b) shows a schematic representation of the typical pattern observed on these surfaces. First, the fracture process is triggered by the nucleation of a crack at a defect in the gauge section. The crack initiation spot can usually be readily located on the surfaces (see micrograph A in Fig. 9(a)). The evolution of the fracture surface pattern agrees with previous observations on epoxy resins (Morgan et al. 1982; Narisawa et al. 1982; Fiedler et al. 2001; Roulin-Moloney 1989) or even on other glassy polymers such as PMMA (Andrews and Reed 1978; Greenhalgh and Hiley 2008). As described in Kausch et al. (2001), the fracture of thermoset polymers follows several distinct stages which are depicted in the central scheme of Fig. 9(b). After the initiation of the crack at a defect, a smooth and featureless region, often referred to as mirror-like, corresponds to the slow propagation of the crack. A textured microflow, such as described by Greenhalgh and Hiley (2008), is also often observed in this first region. Then, the acceleration of the crack leads to a progressively rougher pattern. As the crack propagates, a population of secondary cracks is generated as a result of the high local stress at the vicinity of the primary crack (either due to the presence of secondary defects or to the important local triaxial state of stress near the main crack tip (Manjoine 1971)). The subsequent propagation of these secondary cracks leads to the parabolas observed on the micrographs B and mostly C of Fig. 9(a), as also reported by Fiedler et al. (2001) for uniaxial tension. The final region corresponds to the abrupt fracture of the specimen leading to a much rougher surface without any regular pattern.

The torsion specimens also failed in a brittle manner before any shear banding process, with fracture surfaces oriented at 45° with respect to the specimen longitudinal axis (see Fig. 10(a)), suggesting a failure mode dominated by the maximum principal stress (MPS) value and orientation, confirming previous observations made by Fiedler et al. (2001). The evolution of the pattern observed on the fracture surfaces of the torsion specimens is illustrated in Fig. 9(c). Fracture surfaces for torsion and tension are similar, supporting the idea of a fracture scenario in torsion dominated by principal stresses. Note, however, that next

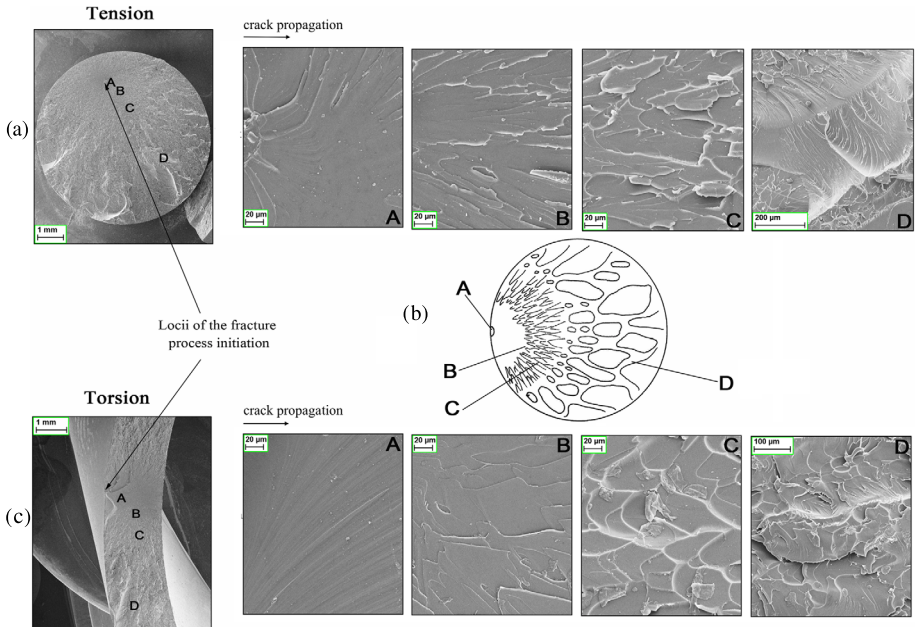


Fig. 9 Detailed fracture surface analysis for tension (a) and torsion (c) test specimens. The schematic (b) is taken from (Cantwell et al. 1988)

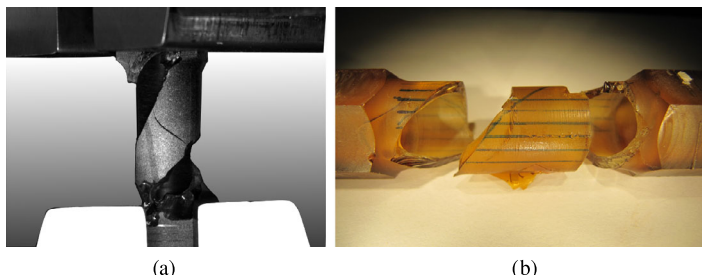


Fig. 10 (a) Hollow tubular specimens loaded in torsion mostly fail along helicoidal surfaces perpendicular to the Maximum Principal Stress (MPS) direction, i.e., oriented at $\pm 45^\circ$ w.r.t. the specimen axis; (b) crack deviation along maximum shear planes is also observed

to the brittle failure associated with normal principal stresses at 45° orientation, the right side of the specimen in Fig. 10(b) indicates a deflection of the fracture path along maximum shear directions, after significant plastic deformation. The simultaneous presence of zones with brittle fracture related patterns and zones involving important plastic deformation in shear was also reported by Fiedler et al. (2001).

Figure 11 shows two typical damage scenarios of a specimen loaded in uniaxial compression. The scenario depicted in Fig. 11(a) shows only a limited accumulation of cracks at the contact zone between the specimen and the platens until the very last instants of deformation. Failure mainly occurs along planes oriented at 45° with respect to the loading direction, suggesting a shear dominated failure mode, causing a sudden failure with a limited number of fragments. The scenario shown in Fig. 11(b) is more frequent. At moderate

Fig. 11 Two different failure scenarios in compression specimen coming from the same batch of bulk resin (same testing temperature and constant strain rate): (a) apparently dominated by maximum shear stress and (b) apparently dominated by the presence of positive MPS

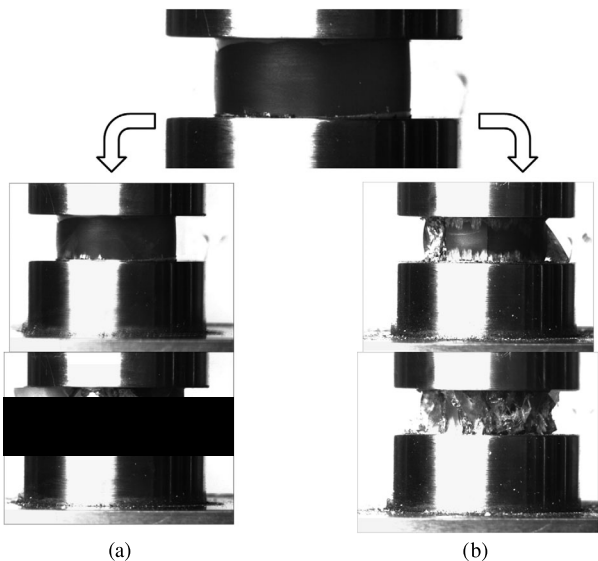
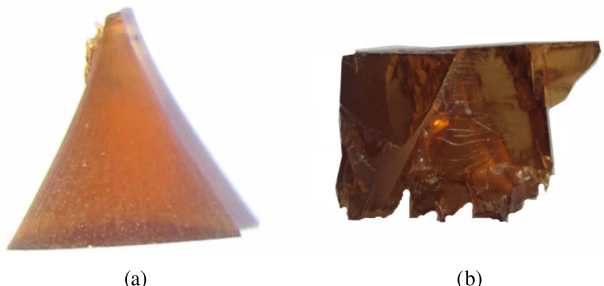


Fig. 12 Uniaxial compression: fragments after failure:
(a) typical conical fragment with rough fracture surface, (b) typical other fragment with essentially mirror-like fracture surfaces



plastic strains, several cracks initiate and propagate in the contact zone, then coalesce with subsequent radial and hoop cracks leading to the formation of a diabolo-shaped chunk, as observed for other brittle materials such as concrete. However, these cracks do not directly lead to the final failure of the specimen. Hence, the final failure of the specimen seems to result from a combination of shear-localization and brittle fracture. The specimen failure is, as in the case of tensile and torsion tests, very sudden with the production of a large number of small fragments.

Figure 12 shows the two main types of fragments observed after failure of the specimen. Figure 12(a) shows the typical cones with rough fracture surfaces, which suggest at least a fraction of shear dominated failure. Figure 12(b) shows an example of fragment with mirror-like surfaces, which is the result of brittle failure perpendicular to a positive MPS. It is not clear whether one mode is more dominant than the other, and which one starts first and possibly triggers the other.

The difference in roughness of the fracture surfaces already visible in Fig. 12 is confirmed by SEM observation in Fig. 13. Again, as seen in Fig. 13(a), the mirror-like surfaces, showing the absence of any topological feature, indicate positive maximum principal stress dominated brittle failure. Conversely, the rough fracture surface observed on the cones along maximum shear direction (see Fig. 13(b)) exhibits a triangular and rhombic morphology.

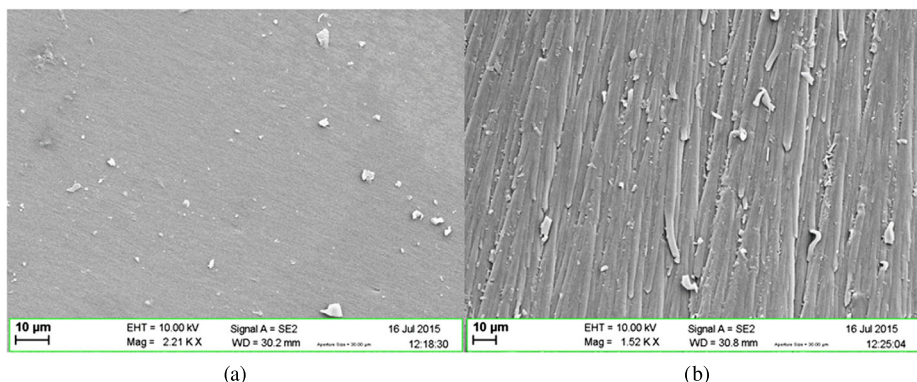


Fig. 13 Fracture surfaces after failure compression specimen examined by scanning electron microscopy: (a) mirror-like fracture surface due to brittle failure, (b) morphology observed on the fracture surface of the conical fragments, in line with the observations by Hobbiebrunken and Fiedler (2007)

While Fiedler et al. (2001) explained this typical morphology by the same mechanism as the one forming the parabolas in tension (nucleation of secondary cracks at defect sites), the 45° orientation of the fracture surface suggests that these rougher surfaces are instead the result of a shear-dominated failure.

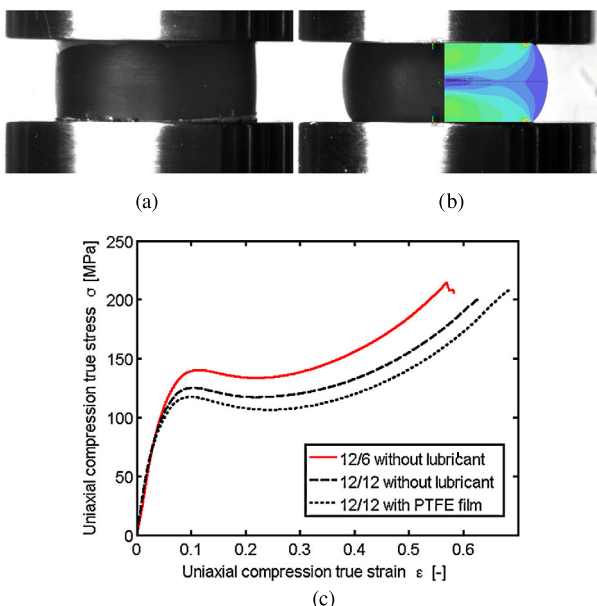
Additional SEM micrographs (not shown) of the fracture surfaces of a complete cone fragment, from tip to basis, provide additional hints on the evolution of the actual fracture process in compression tests and lead to the following conclusions:

- The initiation of the final failure is most probably due to positive MPS, as in the case of tension and torsion;
- The propagation of these initiated cracks can be controlled by the local MPS (longitudinal failure) or by shear stresses when meeting the zones of maximum shear stress (plane at 45° with respect to the loading direction).

4.3 Note on the sensitivity of the uniaxial compression test results to friction

Uniaxial compression tests are known to be sensitive to friction (Liang and Liechti 1996; Gearing and Anand 2004; Fiedler et al. 2001). Friction between the specimen and the platens constrains the lateral movement of the sample, creates a heterogeneous state of stress, which departs from the uniform uniaxial target and can promote or delay the deformation and failure mechanisms. The most visible result of excessive friction between the specimen and the platens is the barreling effect, illustrated in Fig. 14. Figure 14(a) shows a cylindrical sample tested in compression with a PTFE film used as solid lubricant: the specimen lateral edges are almost perfectly straight, proving that friction could be minimized; on the contrary, the specimen in Fig. 14(b) was loaded without any lubricant, and exhibits rounded edges. A map of hydrostatic stress computed using the finite element method and the constitutive model developed in the next sections is superimposed on Fig. 14(b), it reveals large gradients and proves that uniaxial compression tests with significant friction cannot be considered as appropriate to identify the constitutive properties of polymers without the help of inverse analysis procedures. Similar detailed stress analyses of the barreling effect are reported in (Gearing and Anand 2004).

Fig. 14 Sensitivity of the compression test to friction between the sample and the platens: (a) profile of the specimen at large deformation with solid lubricant (PTFE film), (b) typical barrel-like profile of the specimen at large deformation without lubricant, the *color map* shows a distribution of hydrostatic pressure computed using the finite element method, (c) absolute value of the uniaxial true stress versus absolute value of the uniaxial true strain computed from the measured load displacement data with and without solid lubricant for a shape ratio of 12/12, and without lubricant for a 12/6 shape ratio (Color figure online)



Hence, when post-processed with the assumptions of plastic incompressibility and pure uniaxial stress, the constraining effect of friction leads to stress–strain responses which actually erroneously suggest a material that exhibits an apparent stronger behavior than it really is, possibly missing the softening response. By “*apparently stronger behavior*”, it is meant an apparent stress–strain response with artificially higher effective stress. In Fig. 14(c), plots of the absolute values of uniaxial true stress vs. uniaxial true strain show the effect of friction on the apparent compressive behavior of the resin: for similar specimen dimensions, friction provides higher estimates of the peak and lower stresses. Moreover, theoretically, in the absence of friction, the aspect ratio of the specimen should have no effect on the measured stress–strain curve; on the contrary, with friction, increasing the diameter to height ratio leads to an apparently even stronger material, as shown in Fig. 14(c) where the stress–strain curves exhibit higher effective stresses.

5 Constitutive model

5.1 Selection of the constitutive model

The constitutive model was selected in order to be directly compatible with the standard distribution of the general purpose finite element software Abaqus (V6.12 2016), without the need for coding a user defined material subroutine, thereby favoring the application of the identified model in current engineering practice. Nevertheless, the ingredients of the model are chosen so that they can be directly compared or assessed towards more advanced finite strain elastic-viscoplastic models of the literature (Boyce et al. 1988; Tervoort et al. 1996; Poulain et al. 2014). The behavior of the material is assumed to be elastic–plastic with rate and temperature dependencies taken into account through the hardening law. The dependence of the hardening behavior on the strain rate and temperature is given explicitly to Abaqus, which allows for simulating loading rate and temperature effects in the frame

of quasi-static simulations. In its present formulation, the model is not intended for use in the simulation of creep, relaxation or recovery, or for cyclic loading. The selected yield criterion follows a linear Drucker–Prager (Drucker 1953, 1973) model, which is a pressure-modified von Mises yield surface. Isotropic hardening is assumed (consequently preventing the modeling of early reverse plasticity such as, e.g., the Bauschinger effect). An original hardening function incorporating pre-peak yield nonlinearity, softening, and rehardening is developed. Strain-rate and temperature dependencies of the true stress–true strain curve are introduced via the coefficients of the hardening function.

5.2 Yield criterion

The seminal linear Drucker–Prager yield criterion $F(\sigma_e)$ is written as

$$F(\sigma_e) = \sigma_e + \frac{\sigma_{mm}}{3} \tan(\beta) - \left(1 - \frac{\tan(\beta)}{3}\right) \sigma_c = 0 \quad (7)$$

where σ_e is the von Mises stress and σ_c is the yield stress in compression. The term β is the friction angle defined as

$$\tan(\beta) = \frac{3 - 3r}{1 + r}, \quad (8)$$

with the instantaneous uniaxial stress ratio

$$r = \left| \frac{\sigma_t}{\sigma_c} \right| \quad (9)$$

where σ_t and σ_c are the yield stress in uniaxial tension and uniaxial compression, respectively, at an arbitrary uniaxial plastic deformation p . In the linear Drucker–Prager model implemented in Abaqus, no dependence of the hardening behavior on the stress-state is allowed. Hence, the hardening behavior is taken from uniaxial compression tests. Although some strain rate and/or temperature dependence of the friction angle cannot be excluded, they are not taken into account in the model.

5.3 Flow rule

Beside the yield surface, a flow rule is selected based on the flow potential G defined as

$$G = \sigma_e + \frac{\sigma_{mm}}{3} \tan(\varphi) \quad (10)$$

where φ is the “dilation angle” in the $(\sigma_e, -\frac{\sigma_{mm}}{3})$ plane. Setting $\varphi = \beta$ results in associated plastic flow. With $\varphi = 0$, plastic incompressibility is assumed. The dilation angle at a given plastic strain p is computed as

$$\tan(\varphi) = -\frac{3(1 - 2\nu_p^c)}{2(1 + \nu_p^c)} \quad (11)$$

where ν_p^c is the plastic Poisson coefficient measured in compression given by $\nu_p^c = \frac{p_r^c}{p_z^c}$ with p_r^c and p_z^c being the radial and axial plastic strains under uniaxial compression, respectively. As previously defined in Eq. (1), the plastic strain tensor is

$$p_{ij} = \varepsilon_{ij} - S_{ijkl} \sigma_{kl} \quad (12)$$

where ε_{ij} is the logarithmic or Hencky strain tensor, σ_{kl} is the Cauchy stress tensor, and S_{ijkl} is the elastic compliance tensor. Although some strain rate and/or temperature dependence of the dilation angle cannot be excluded, they are not taken into account in the model.

5.4 Elastic behavior

The resin is isotropic with Young's modulus E and Poisson ratio ν . For the sake of simplicity, the Poisson ratio is taken as rate and temperature insensitive. The asymmetry of Young's modulus between tension and compression is neglected and, as a first approximation, the experimental compression modulus is used. The compression modulus is assumed to take the form

$$E\left(T, \left(\frac{dp}{dt}\right)\right) = \bar{E}(293)e^{\beta_T(T-293)} + k_\varepsilon \left(\ln\left(\left(\frac{dp}{dt}\right)\right) - c_\varepsilon \right) \quad (13)$$

where $\bar{E}(293)$ is the compression modulus averaged over all strain rates at room temperature, c_ε is the average of the logarithms of all the tested true strain rates, β_T and k_ε are fitting parameters. The identified strain-rate dependence of the Young's modulus should hold up to strain rates of 100 s^{-1} according to Gerlach et al. (2008).

The strain rate dependence of the Young's modulus in equation (13) refers to the average effective plastic strain rate. This apparent contradiction with the theory of plasticity is justified by the will to keep the convention followed in the rest of the paper where all the dependencies on strain rate indeed refer to the average effective plastic strain rate. In most quasi-static loading situations, however, the dependence on strain-rate could even be neglected, taking $k_\varepsilon = 0$.

5.5 Hardening behavior

The strain hardening is assumed not to depend on the stress triaxiality, which can be admitted for small to moderate strains; however, in general, the rehardening part (stage IV in Fig. 1) can be highly sensitive to the hydrostatic stress. Poulain et al. (2014) showed that the hardening behavior of a moderately crosslinked epoxy is different in tension and compression on the whole range of strain. The dependence on pressure of the element analogous to entropic resistance is thus not accounted for in the model.

The hardening law (σ_y) is described by a sum of three contributions: (i) the pre-peak hardening behavior ($\sigma_{0.002} + \sigma_A$) related with the main chain segmental motion activation, (ii) the softening part σ_B coming from collective activated conformational motions combined with free volume rearrangement (Jatin et al. 2013) and then (iii) the rehardening σ_C often referred to as the “entropic spring” contribution. This approach, illustrated in Fig. 15, is inspired by the pioneering work of Haward and Thackray (1968).

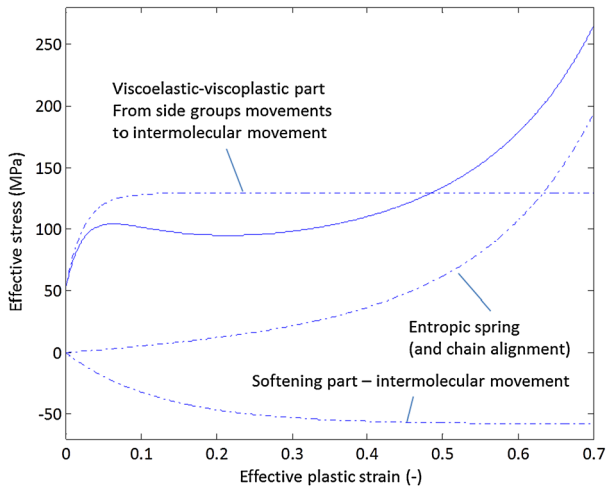
The present formulation relies on the commonly accepted understanding of the molecular motion of entangled or crosslinked glassy polymers during straining. Below the glass transition temperature, in order to achieve large plastic strain, the polymer has to overcome two main types of physical-mechanical resistance: the intermolecular resistance ($\sigma_{0.002} + \sigma_A + \sigma_B$) and the term analogous to the entropic resistance $\sigma_{C_{11}}$.

At low strains, the polymer has to be loaded above the stress $\sigma_{0.002}$ (and with an appropriate stress triaxiality) in order to exceed the activation energy for segmental rotation. The contribution of this mechanism to the hardening of the polymer is denoted σ_A and is expressed as

$$\sigma_A = \sigma_{A0} \left(1 - e^{-r_A p}\right) \quad (14)$$

where σ_{A0} is the overstress targeted plateau and r_A is a fitting parameter driving the hardening rate.

Fig. 15 Decomposition of the hardening curve (continuous line) into three main contributions (dot-dashed lines): $(\sigma_{0.002} + \sigma_A)$, σ_B , and σ_C



The contribution of softening to the hardening of the polymer is denoted σ_B and given by

$$\sigma_B = \sigma_{B0}(1 - e^{-r_B p}) \quad (15)$$

where σ_{B0} is the yield drop targeted plateau and r_B is a fitting parameter driving the softening rate.

At larger strains, a simple exponential function of p could be chosen in order to model rehardening. Nevertheless, in this case, it would be more difficult to compare the identified parameters with those obtained with more advanced finite strain models which introduce an entropic spring formulation to model rehardening and backstress effects. Therefore, the latest contribution to the hardening is taken as analogous in mathematical form to the entropic resistance due to the alignment of the molecular network, although it does not play the role of backstress anymore and is built upon the plastic deformation gradient. This contribution is thus borrowed from the Arruda–Boyce 8-chain model of rubber elasticity (Arruda and Boyce 1993),

$$\sigma_C = \frac{C_R}{3} \frac{\sqrt{N}}{\lambda_p} \mathcal{L}^{-1} \left(\frac{\lambda_p}{\sqrt{N}} \right) \text{dev}(\mathbf{B}) \quad (16)$$

where C_R is the hardening modulus (C_R is the rubbery modulus for the material in the rubbery state), \sqrt{N} determines the limiting chain extensibility, N being the number of links in a chain, $\mathbf{B} = \mathbf{F}\mathbf{F}^T$ is the left Cauchy–Green tensor and $\text{dev}(\mathbf{B})$ its deviator. To translate this into a contribution to the hardening law, the left Cauchy–Green tensor is replaced by its plastic component (assuming an additive decomposition of the deformation gradient), i.e., $\mathbf{B}_p = \mathbf{F}_p \mathbf{F}_p^T$ with \mathbf{F}_p the plastic deformation gradient (assuming plastic incompressibility)

$$\mathbf{F}_p = \begin{pmatrix} e^{p_{11}} & 0 & 0 \\ 0 & e^{p_{22}} & 0 \\ 0 & 0 & e^{p_{33}} \end{pmatrix} = \begin{pmatrix} e^p & 0 & 0 \\ 0 & e^{-0.5p} & 0 \\ 0 & 0 & e^{-0.5p} \end{pmatrix}. \quad (17)$$

The term λ_p is the stretch on a chain of the 8-chain network defined as

$$\lambda_p = \sqrt{\frac{B_{p,mm}}{3}}. \quad (18)$$

The symbol \mathcal{L}^{-1} represents the inverse Langevin function, which is here approximated by the Cohen rounded Padé approximation (Cohen 1991)

$$\mathcal{L}^{-1}(y) = y \frac{3 - y^2}{1 - y^2}. \quad (19)$$

Other expressions for the rehardening could be assumed, considering, for instance, a Neo-Hookean behavior, a 3-chain or 8-chain model or the full-chain model by Wu and van der Giessen (1993). Note that entropic springs such as the 8-chain model detailed in the expression of σ_C imply the existence of transverse stresses that should be iteratively removed by applying an appropriate transverse strain in order to recover pure uniaxial conditions; the present model overlooks this effect by taking into account the axial component of σ_C only. First, the impact of neglecting the transverse stresses brought by the entropic spring is that the identified parameters will be slightly different. Second, considering the spring as a simple hardening function relating the effective stress and the effective or equivalent plastic strain cancels the “multi-axial contribution” and inherent pressure-sensitivity.

The yield stress hardening law (σ_y) of the resin can then be expressed as

$$\sigma_y = \sigma_{0.002} + \sigma_{A0}(1 - e^{-r_A p}) + \sigma_{B0}(1 - e^{-r_B p}) + \sigma_{C_{11}} \quad (20)$$

where $\sigma_{C_{11}}$ is the axial component of the rehardening stress. Because of the underlying thermally and stress activated deformation mechanisms, the strain-rate and temperature dependence of the stress parameters $\sigma_{0.002}$ and σ_{A0} is assumed to follow the Eyring's equation, i.e.,

$$\sigma_i = \frac{k_B T}{\Omega_{A_i}} \left(\ln \left(\frac{dp}{dt} \right) - \ln(\dot{p}_0) \right) + \frac{\Delta G}{N_A \Omega_{A_i}} \quad (21)$$

with $i = 0.002$ or $i = A0$ and N_A is the Avogadro number. Inspired by the work of (Boyce et al. 1988) where the saturation stress is taken as a constant fraction of the “athermal shear strength”, the strain rate and temperature dependence of σ_{B0} is introduced through $\sigma_{B0} = -k\sigma_U$ where k is a strain-rate and temperature insensitive fitting parameter named “yield drop coefficient” while σ_U is the strain-rate and temperature dependent peak stress, which also obeys Eyring's equation. The parameters r_A and r_B governing the pre-peak hardening rate and the softening rate are taken as

$$r_A = r_{A,a} T^{n_A} + r_{A,b} \quad (22)$$

and

$$r_B = r_{B,a} T^{n_B} + r_{B,b}. \quad (23)$$

In line with the approach of Arruda and Boyce (1993), C_R appearing in equation (19) is assumed independent of strain rate and temperature. Then \sqrt{N} is taken independent of strain-rate while its sensitivity to temperature is expressed as

$$N(T) = \frac{n(293)N(293)}{B_h + A_h(1 - e^{-\frac{E_h}{k_B T}})} \quad (24)$$

where $n(T)$ is the chain density at temperature T , E_h is the thermal dissociation energy, and A_h and B_h are fitting parameters. This last formula expresses the fact that the number of efficient rigid links per chain $n(T)N(T)$ remains constant whatever the temperature. Alternatively, for materials below the glass transition temperature, Rottler (2009) and Govaert et al. (2008) indicate that the hardening modulus C_R should depend linearly on the yield stress (hence having the same strain-rate and temperature sensitivities) and on the hydrostatic pressure.

Table 2 List of the parameters of the constitutive model

Variable	Parameters
Modulus	$\beta_T, k_\varepsilon, \bar{E}(293), c_\varepsilon$
Poisson ratio	ν
Stress ratio	r
Plastic Poisson ratio	ν_p^c
Activation volumes	$\Omega_{A_U}, \Omega_{A_{0.002}}, \Omega_{A_{A0}}$
Activation enthalpies	$\Delta G_U, \Delta G_{0.002}, \Delta G_{A0}$
Reference transformation rates	$\dot{p}_{0U}, \dot{p}_{0.002}, \dot{p}_{0A0}$
Yield drop coefficient	k
Hardening kinetics coefficients	$r_{A,a}, r_{A,b}, n_A$
Softening kinetics coefficients	$r_{B,a}, r_{B,b}, n_B$
Rubber modulus	C_R
Efficient chain segments	$A_h, B_h, E_h, N(293)$

5.6 Parameter identification

Table 2 summarizes the parameters that must be identified. Some parameters can be directly identified from the experimental results, while others are identified through a reverse engineering procedure. The minimum set of experiments must involve four compression tests, e.g., two tests at different CSR and room temperature, and two tests at different temperatures, whatever the selected strain rate and one tensile test at room temperature and at a CSR (for which a room temperature compression test is also available).

The identification of the model parameters is made through a two-step procedure:

- Several model parameters (13) can be identified directly against the experimental results: the modulus parameters $\beta_T, k_\varepsilon, \bar{E}(293), c_\varepsilon$, the Poisson ratio ν , the stress ratio r , the plastic Poisson ratio ν_p^c (at room temperature, at an effective plastic strain of 3 %), the stress parameters for $\sigma_{0.002}$ and σ_U (i.e., the activation volumes, enthalpies and reference transformation rates that appear in Eyring's equation (21)).
- The remaining model parameters (15) are identified by minimizing the distance between the predicted compression true stress–true plastic strain curves and the reference experimental data points shown in Fig. 1. Additionally the slope of the stress strain curve should be zero at the peak and lower stresses. A gradient based optimizer provided in Matlab (R2015 2015) is used for that purpose.

Table 3 shows the values identified for the parameters of the constitutive model.

The identified activation volumes are in the same range as those reported in (Gómez-del Río and Rodríguez 2012) for a DGEBA epoxy resin. The main parameters of the rehardening part (C_R, N) are also comparable with values reported in the literature for other glassy polymers (Arruda and Boyce 1993; Poulain et al. 2014).

The effective stress–effective plastic strain curves resulting from the identification procedure are shown in Fig. 16(b), with representative experimental results reproduced in Fig. 16(a) for the sake of comparison. A good agreement is found in terms of capability to reproduce the hardening behavior in the studied range of strain rates and temperature. Note that the resulting stress–strain curves are “predictions” for all but the reference points used for identification.

Table 3 List of parameter values identified for the constitutive model

Parameter	Values	Parameter	Values
β_T	-0.00261 K^{-1}	$\Omega_{A0.002}$	$2.31 \cdot 10^{-18} \text{ mm}^3$
k_ε	$30.64 \text{ MPa} \cdot \text{s}$	$\Omega_{A_{A0}}$	$2.43 \cdot 10^{-18} \text{ mm}^3$
$\bar{E}(293)$	2587 MPa	C_R	26.6 MPa
c_ε	-5.86 s^{-1}	A_h	$9.52 \cdot 10^{35}$
ν	0.34	B_h	$11 \cdot 10^{31}$
r	0.855	E_h	8 J/mol
$v_p^c(p=0.03)$	0.5	$N(293)$	1.87
ΔG_U	$2.86 \cdot 10^5 \text{ J/mol}$	k	0.954
$\Delta G_{0.002}$	$2.06 \cdot 10^5 \text{ J/mol}$	$r_{A,a}$	$1.023 \cdot 10^{-10} \text{ K}^{-1}$
ΔG_{A0}	$4.76 \cdot 10^5 \text{ J/mol}$	$r_{A,b}$	35.88
$\dot{p}_0 U$	$2.83 \cdot 10^{23} \text{ s}^{-1}$	n_A	4.63
$\dot{p}_0 0.002$	$3.04 \cdot 10^7 \text{ s}^{-1}$	$r_{B,a}$	$3.4 \cdot 10^{-20} \text{ K}^{-1}$
$\dot{p}_0 A_0$	$8.79 \cdot 10^{49} \text{ s}^{-1}$	$r_{B,b}$	2.15
Ω_{AU}	$1.09 \cdot 10^{-18} \text{ mm}^3$	n_B	7.54

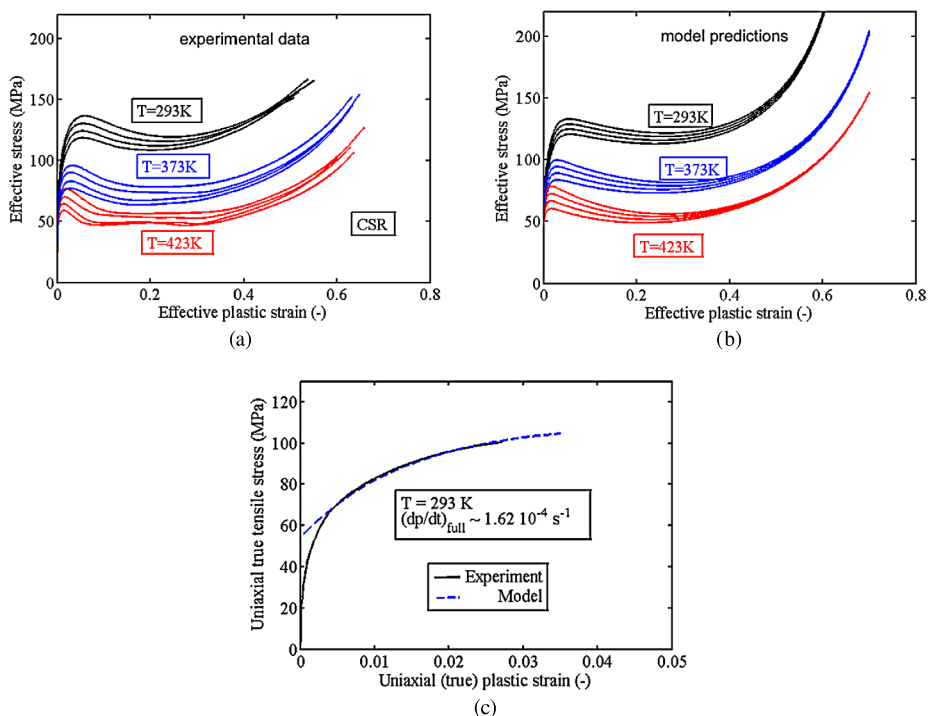
**Fig. 16** (a) Experimental compression curves obtained with constant strain rate tests, (b) predicted compression curves using the hardening law identification procedure, and (c) uniaxial behavior predicted in tension, obtained by multiplying the uniaxial hardening curve identified in compression (for the same temperature and strain rate conditions) by the stress ratio identified at 0.03 effective plastic strain

Figure 16(c) shows the behavior predicted in tension, obtained by multiplying the hardening curve identified in compression (for the same temperature and strain rate conditions) by the stress ratio identified at a 3 % effective plastic strain.

5.7 Constitutive model as implemented in Abaqus

First, concerning the linear elastic behavior, the asymmetry of elastic modulus is neglected, the dependence of the modulus on the strain-rate is not taken into account, and the Poisson ratio is assumed constant. Therefore, tabulated pairs of elastic modulus and temperature are provided to the code Abaqus.

Second, the linear Drucker–Prager model is selected, and the friction and dilation angles identified in the previous section are specified. The hardening behavior is introduced in Abaqus by providing tables of pairs of von Mises stress and equivalent plastic strains (i.e., the hardening curves in compression) at different strain-rates and temperatures. In this context, Abaqus requires a virtual “zero strain rate” hardening response, which can, for instance, be arbitrarily taken as the curve predicted by the constitutive model at a plastic strain rate of, e.g., 10^{-12} s^{-1} . Abaqus interpolates linearly between the curves provided by the user, but keeps the highest strain-rate hardening curve provided by the user if the computed strain-rate exceeds this highest value of maximum strain-rate. The model introduced in Sect. 5 implies that the shape of the yield surface in the deviatoric plane is circular, which is one particular case of the linear Drucker–Prager criterion implemented in Abaqus. In this case, the ratio of the yield stress in triaxial tension to the yield stress in triaxial compression is set to one, which is the default value.

The model is thus readily available in Abaqus. In certain circumstances or high stress triaxialities within heterogeneous stress fields (e.g., around stress concentrations), the standard quasi-static nonlinear finite element solver could exhibit very slow convergence due to some instability of the resolution scheme for the linear Drucker–Prager model. In these occasions, the user might have to change to fully explicit simulations, with appropriate mass scaling and viscosity, to reach a consistent, converged solution.

5.8 Validation of the constitutive model

The predictive capability of the identified model is assessed against experimental results which were not used for parameters identification, i.e.,

- The hardening behavior in shear at room temperature, obtained by torsion testing of hollow cylindrical specimens at a rotation rate of $7^\circ/\text{min}$. Figure 17(a) shows the responses identified in compression and tension, and the prediction of the model for the case of torsion. Despite minor differences of experimental plastic strain rates, the prediction for shear is equidistant from the compression and tension curves due to the hypothesis of linear dependence of yielding on the hydrostatic pressure, and falls close to the curve representative of shear loading.
- The hardening behavior in tension at temperatures of 373 and 423 K and a CCDR of 1 mm/min; Fig. 17(b) shows the predictions of the model in terms of the tensile behavior at higher temperatures. The agreement is here not very good, as the stress ratio identified at room temperature seems to be temperature dependent. Hence, the tension–compression asymmetry is underestimated at 373 and 423 K.

The tension–compression asymmetry being attributed to the different behavior of free volume under tensile and compressive stresses and the evolution of this free volume (movement, creation, and annihilation) being thermally activated, it is reasonable to think that

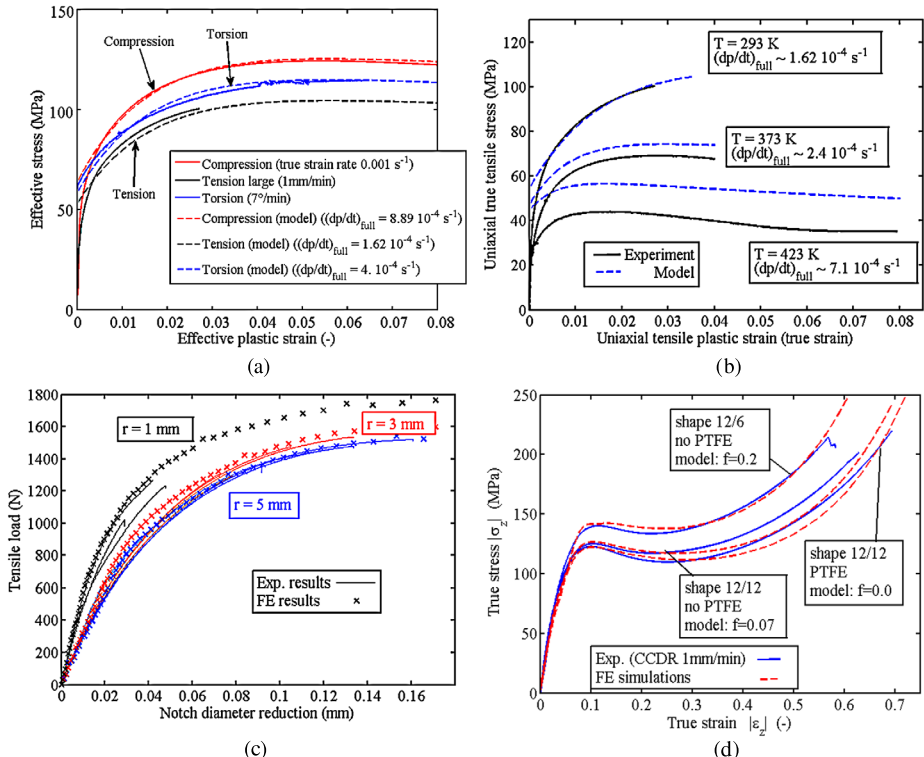


Fig. 17 Constitutive model assessment: (a) “Effective stress versus effective plastic strain” curves for uniaxial compression, tension, and for torsion, predicted using the identified hardening law and the identified pressure dependence of yielding (linear Drucker–Prager); (b) predicted temperature dependence of yielding under tensile loading, note the apparent dependence of pressure sensitivity on temperature; (c) variation of the load with the reduction of diameter of the minimum cross-section for three different notch radii and a constant crosshead displacement rate of 1 mm/min; and (d) prediction of the apparent compression stress–strain curves (absolute values) with and without solid lubricant, and for different cylinder diameter/height ratios

an additional temperature dependence of the stress ratio should be incorporated instead of a non-temperature-dependent Drucker–Prager model.

- The nonlinear relationship between the diameter reduction in the minimum cross-section and the tensile load on the tensile tests conducted on notched specimens at a CCDR of 1 mm/min, at room temperature, for three different notch radii. In this case, explicit simulations were performed using Abaqus v6.12 in order to properly account for the important heterogeneity of hydrostatic stress and strain-rate in the gauge length. Figure 17(c) reveals a very good agreement between the FE results and the experimental data for the three notch radii.
- The compression true stress–true strain curves obtained at room temperature and a 1 mm/min CCDR with different conditions of friction with the platens. Chevalier et al. (2016) have shown that a friction coefficient of 0.07 is necessary in order to satisfactorily reproduce the barreling profile using FE simulation with the model presented in this section. Figure 17(d) shows that the FE simulation of the compression test without lubricant, for a similar diameter to height ratio (12/12), is remarkably close to the corresponding apparent experimental curve.

Note that the discrepancies in the nonlinear hardening behavior could partly be attributed to batch to batch variability as the model was identified on another batch. Increasing the diameter to height ratio (e.g., here 12/6) makes the constraining effect of friction more prominent. Hence, the friction coefficient must be increased to 0.2 in order to capture the experimental behavior. In this case, part of the error lies in the inability of the model to deal with larger stress gradients and another part in the too simplistic modeling of friction.

6 Failure criterion

6.1 Preamble

No detectable damage evolution is observed in RTM6. Despite significant nonlinear deformation, there is no evidence of intrinsic progressive damage mechanisms such as void growth and coalescence observed for instance in ductile metals or blended polymer, or crazing which is commonly observed in thermoplastics (Kinloch and Young 1983; Haward and Bowden 1973). Hence, in Sect. 4.2, no microstructural features or morphologies on the fracture surfaces could be associated with an intrinsic progressive damage mechanism or extensive plasticity. No progressive drop of the Young's modulus is observed either, which could have been considered as an indirect proof of damage incurred in the specimen. Furthermore, Morelle (2015) observed on the same resin a rapid saturation of the backstress upon unloading, which is another argument in favor of the idea of the absence of progressive damage. Hence, failure appears to be brittle in all circumstances (tension, notched-tension, torsion, and compression) whatever the amount of plastic deformation. This is in-line with the researches reported in Asp et al. (1996), Hobbiebrunken and Fiedler (2007), Fiedler et al. (2001, 2005) which converge to the idea of a competition between shear-dominated yielding and brittle failure driven by a positive hydrostatic and/or MPS related with micro-cavitation and chain scission. The brittle character of failure is most probably due to the high crosslinks density which impedes the very large molecular movements at the local scale which is necessary to achieve a configuration of crazing. Andrews and Reed, in a paper on the kinetic theory of fracture (Andrews and Reed 1978), report that failure in thermoset resins occurs by chain scission when the stress in some segments of the molecular network reaches a critical value, essentially at the locus of small defects which act as stress concentrators. This approach is also followed by Chevalier et al. (2016) who claim that failure in highly crosslinked epoxies is driven by the occurrence of a given MPS at the locus of an ellipsoidal void in the resin.

In this paper, failure has been addressed based on an uncoupled approach as a post-processing task, considering that fracture occurs when some combination of stress or strain reaches a critical value, and that cracking is catastrophic, with almost no dissipation after damage initiation.

6.2 Failure criteria

Four different macroscopic failure criteria, written in a generic form as $f(\sigma_{ij}) = 0$ or $f(p_e) = 0$, have been selected and assessed:

- FC-I. In-line with the common understanding of brittle failure in highly-crosslinked epoxies, the first criterion considers that failure occurs when a pressure-modified maximum principal stress is reached:

$$(FC-I) \quad \sigma_{MAX} - a\sigma_H - b = 0. \quad (25)$$

This criterion can be easily identified using the failure stress data in tension and compression.

- FC-II. The second criterion is a hyperbolic criterion, similar in form to some crazing initiation criteria as reviewed in Gearing and Anand (2004):

$$(FC-II) \quad \sigma_e - \frac{a}{\sigma_H + b} - c = 0. \quad (26)$$

This criterion is actually a pressure-modified “critical distortional strain energy criterion.” The three parameters must be identified using the failure stress data in tension, compression, and torsion.

- FC-III. The third criterion is a pressure-modified maximum shear criterion, similar to a pressure-modified Tresca criterion, motivated by the occasional observation of a shear-dominated failure mode as observed in Fig. 11(a):

$$(FC-III) \quad |\sigma_{MAX} - \sigma_{MIN}| - a\sigma_H - b = 0. \quad (27)$$

This criterion can be easily identified using the failure stress data in tension and compression

- FC-IV. The fourth criterion is a triaxiality-dependent critical equivalent plastic strain at failure criterion, often used in the modeling of the ductile failure of metals:

$$(FC-IV) \quad p_e - ae^{-b\frac{\sigma_e}{\sigma_H}} - c = 0. \quad (28)$$

The three parameters can be identified using the failure stress data in tension, compression, and torsion.

6.3 Parameter identification and validation

The parameters of the four failure criteria have been identified directly using the experimental failure stress data, see Table 4.

Table 4 Parameter values identified for the four failure criteria

Criterion	a	b	c
FC-I	1064 [-]	66 [MPa]	–
FC-II	5352 [MPa]	105.7 [MPa]	63 [MPa ²]
FC-III	−0.8824 [-]	132 [MPa]	–
FC-IV	0.04042 [-]	7.815 [-]	0.02558 [-]

Figures 18(a)–(c) show the variation of each stress indicator $f(\sigma_{ij})$ as a function of the hydrostatic stress, for failure criteria FC-I, FC-II, and FC-III, while failure criterion FC-IV is presented with the evolution of equivalent plastic strain at failure as a function of the stress-triaxiality in Fig. 18(d). FC-I and FC-III can be assessed by comparing the predicted failure stress in torsion with the experimental value, as the latter was not used for identification, showing excellent agreement.

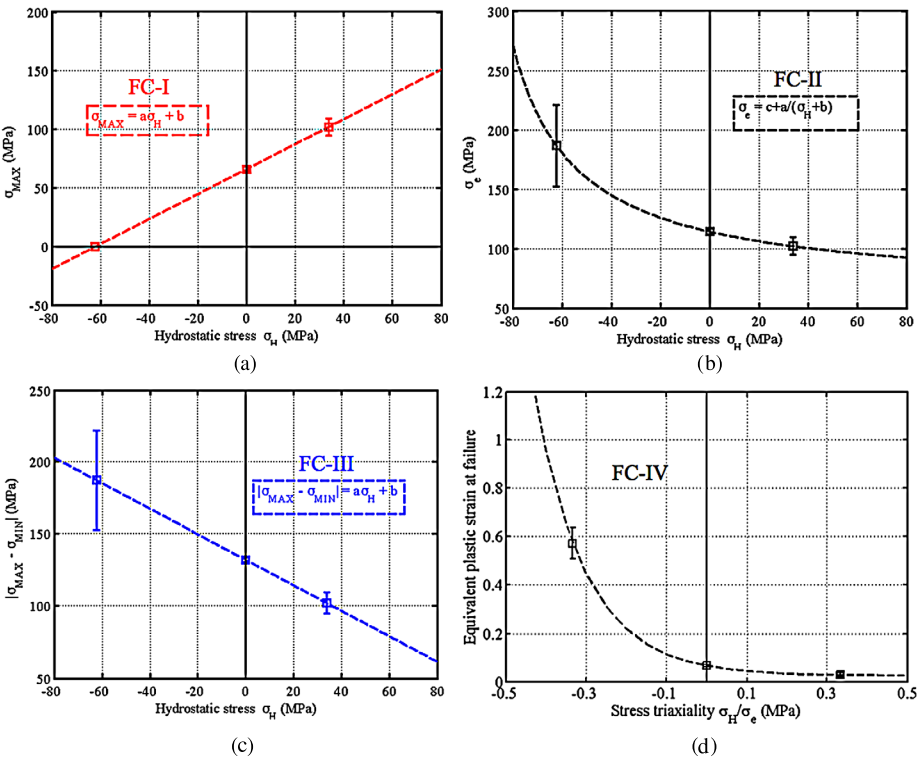


Fig. 18 (a) Pressure-dependent critical maximum principal stress failure criterion (FC-I) identified with the compression and tension data, (b) pressure-dependent critical von Mises stress failure criterion (FC-II) identified with the compression, tension, and torsion data, (c) pressure-dependent critical maximum shear stress failure criterion (FC-III) identified with the compression and tension data; and (d) critical equivalent plastic strain at failure criterion (FC-IV) identified with the compression, tension, and torsion data

The four failure criteria were used in combination with the constitutive model in FE simulations of the notched tensile tests in order to predict the maximum load and notch diameter reduction at failure.

For the maximum load at failure, Fig. 19(a) shows that all but the pressure-modified MPS criterion FC-I predict an increase of the load with an increasing notch radius. The pressure-modified maximum shear stress criterion FC-III significantly underestimates the various loads. Despite the fact that it does not reproduce the correct load evolution with notch radius, criterion FC-I falls within the experimental variability for the 1 and 3 [mm] notch radii. On the other hand, the triaxiality-dependent equivalent plastic strain at failure FC-IV performs very well, as its predictions for the failure load are the closest to the average experimental values, as illustrated in Fig. 19(a).

In terms of notch radial displacement at failure as shown in Fig. 19(b), all the criteria correctly predict the increase of notch diameter reduction with increasing notch radius, and it is again the triaxiality-dependent plastic strain at failure criterion FC-IV which performs the best. The pressure-modified MPS criterion performs also quite well.

In conclusion, if all identified fracture criteria seem to qualitatively reproduce the experimental failure trends, the triaxiality-dependent plastic strain at failure FC-IV is the only

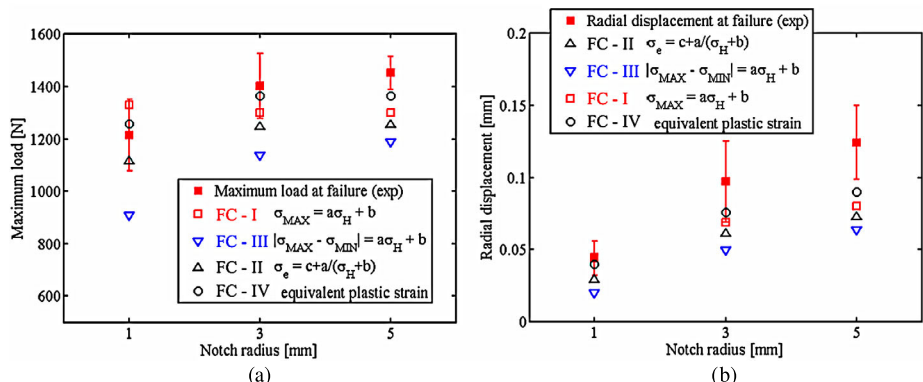


Fig. 19 Model assessment (nonlinear behavior and failure) against experimental results on notched tensile tests: **(a)** experimental versus predicted failure load and **(b)** experimental versus predicted radial displacement in the notch (local striction)

one to provide fully quantitative predictions and is therefore chosen as the most relevant criterion.

Criterion FC-IV is readily introduced in Abaqus using “Ductile fracture criterion” capability. Pairs of effective (or equivalent) plastic strain at failure and stress triaxiality must be provided, for different temperatures and strain-rates. In this case, the failure criterion was provided at a reference strain-rate of 10^{-3} s⁻¹ and a temperature of 293 K, assuming first that failure is independent of strain-rate. This allows simulating crack initiation in deformed components.

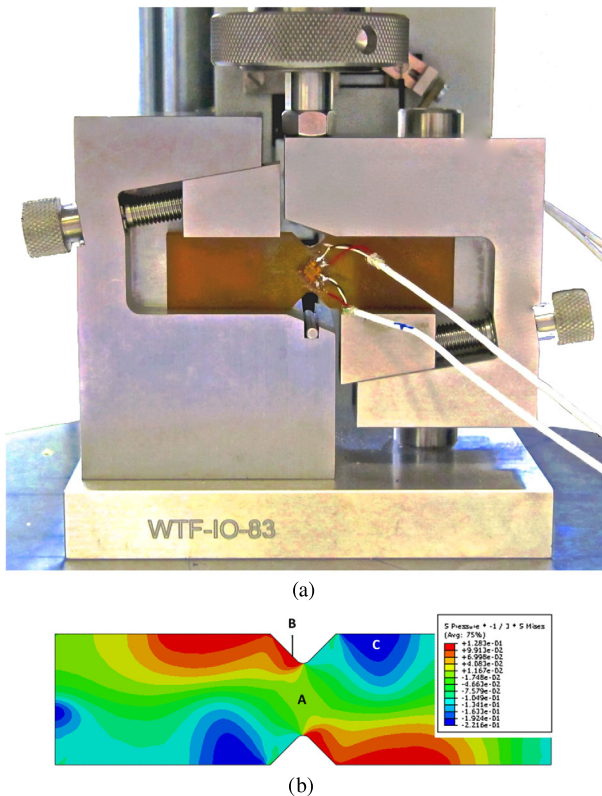
7 Full model assessment—Iosipescu case study

The original motivation of this work is to build, identify, and assess a model that can be used in the framework of the multi-scale modeling of the deformation and failure of carbon-epoxy composites where highly heterogeneous stress and strain fields are encountered. However, before addressing this level of complexity, it is important, in terms of methodology, to first assess the model against a simpler configuration where the field heterogeneity is moderate but with a clear contrast between zones with distinct shear-dominated and hydrostatic stress/maximum principal stress dominated conditions.

The test selected for validation comes from the ASTM5379 V-notched beam method, with set-up and sample illustrated in Fig. 20(a). The V-notched beam method is, in principle, dedicated to the measurement of the shear properties of composite materials with continuous or short fibres (Hodgkinson 2000). Hence, a good portion of the ligament between the V notches undergoes uniform shear stresses. However, as depicted in the stress triaxiality map right before failure in Fig. 20(b), although most of the deformed zone is the shear-dominated zone A, high tensile stresses are generated at the surface close to the notch roots (zone B), while compressive stresses are induced at the end of the contact zone with the load fixture (zone C). With an unreinforced isotropic material, this test is somehow critical as the nonlinear behavior should be mostly determined by the response in shear between the notch roots, while failure should be triggered elsewhere.

The V-notched beam specimens were produced with the processing and machining conditions described in Sect. 2. A series of five tests were performed on a screw-driven universal

Fig. 20 (a) The V-notch beam test sample instrumented with back-to-back bidirectional strain gauges, and load introduction fixture. (b) Map of stress triaxiality on the V-notch specimen just before failure: zone A is the shear-dominated zone (triaxiality close to zero), zone B is dominated by tensile stresses and exhibits the maximum triaxiality (above 1.2), and zone C is essentially compressive



Zwick–Roell testing machine with an external load cell of 250 kN, at 293 K and a crosshead displacement rate of 1 mm/min. The maximum and minimum principal strain were measured using back-to-back bi-directional strain gauges positioned between the notch roots at 45° with reference to the horizontal axis.

A two-dimensional explicit finite element model was set-up in Abaqus 6.12 to simulate the test, with a global mesh size of 0.5 mm, using linear triangular plane stress elements. A local mesh size of 0.1 mm was imposed at the notch roots. Frictionless contact was assumed. The constitutive model was introduced as explained in Sect. 5.7. The failure criterion FCIV identified at room temperature and a strain rate of 10^{-3} s⁻¹ in Sect. 6.2 was introduced in Abaqus as explained in Sect. 6.3. The effective plastic strain at failure initiation is specified at different stress triaxialities, and Abaqus interpolates between these values. In addition to that, progressive failure analysis, using a smeared crack approach, was enabled by using the “Damage Evolution” feature of the “Ductile failure criterion” with an exponential softening law, given an arbitrary “post-initiation fracture” energy of 1 mJ. Once damage has initiated, the degradation evolves according to the energy dissipated in the fracture process. The computed degradation (between 0 and 1) corresponds to the fraction of the total fracture energy already dissipated. Once one integration point inside one element has reached the maximum degradation (set here to 0.99), this element is removed. Besides, appropriate mass scaling was used in order to accelerate the simulations while not perturbing the solution.

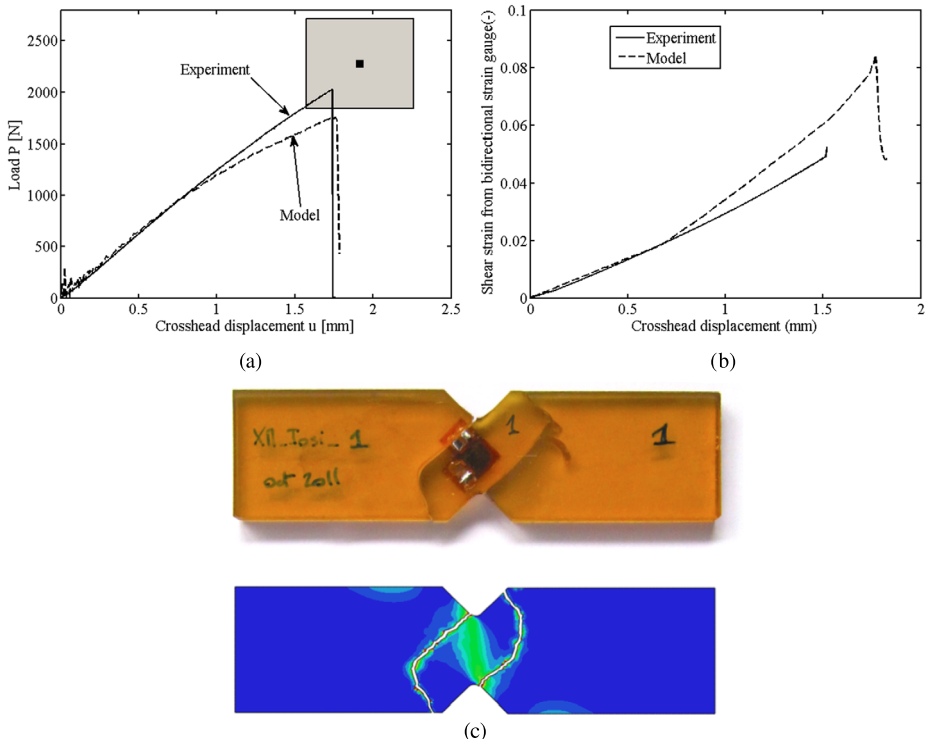


Fig. 21 (a) Experimental representative load–displacement curve between the notch roots and predicted counterpart. The grey rectangle is the error box for the pair experimental load at failure—displacement at failure; (b) comparison of the shear strain measured experimentally between the notch roots (representative curve) and the computed shear strain averaged over the strain gauge area in the FE model; and (c) comparison of the experimental (TOP) and predicted crack paths (BOTTOM). The bottom image shows a map of the value of the failure criterion, the elements which have failed have been deactivated and eventually constitute the crack path

The model is assessed against experimental results as follows:

- The predicted and experimental load–displacement curves, maximum load and displacement at failure are compared (see Fig. 21(a)). Good agreement is found although the predicted load at failure falls below the error box.
- The predicted and experimental shear strain at the locus of the strain-gauge between the notch roots are compared (see Fig. 21(b)). Good agreement is found regarding the linear part of the measured shear strain, however, after the onset of plasticity, the prediction overestimates the experimental response by up to 20 %.
- The predicted and observed failure hierarchy and final crack path are compared (Fig. 21(c)). Excellent agreement is found, in-line with the failure mode observed by Hodgkinson (2000) for unreinforced brittle thermoset materials.

The explanation for the underestimation of the load at yielding and for the overestimation of the nonlinearity is four-fold:

- Early plasticity is predicted in the simulation in the stress concentration areas located at the end of the contact zone between the load introduction rig and the sample (zone C in

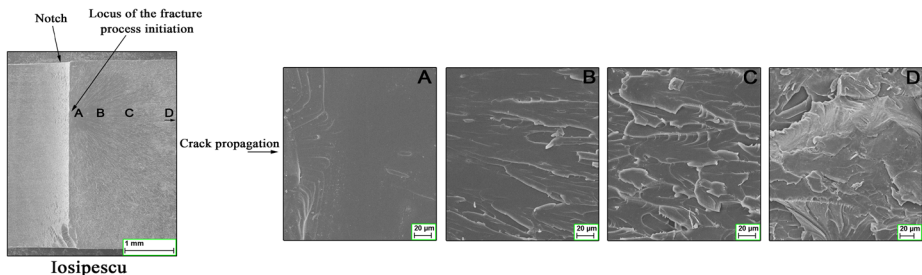


Fig. 22 Detailed fracture surface analysis after failure of the V-notch beam specimen

Fig. 20(b)). This stress concentration favors a “root rotation” of the shear dominated zone and lead to an overestimation of the specimen tangent compliance.

- The absence of friction in the simulations accelerates the onset of yielding and leads to a more compliant overall response. Hence, adding friction between the load introduction rig and the sample in the simulation helps delaying the onset of yielding, but not sufficiently. Note that the experimental maximum and minimum principal strains measured by the strain gauge are slightly asymmetric (up to 10 % of difference); according to the simulations, this asymmetry increases with increasing friction.
- Part of the discrepancy might be attributed to batch-to-batch variability which is known to be of up to 10 % for the peak stress in compression.
- The constitutive model overestimates (either or both) the strain-rate sensitivity (note the equivalent plastic strain rate in the simulation ranges between 0.0002 and 0.0008 s⁻¹) and the pressure sensitivity of yielding of the material.

Finally, it is worth mentioning that fracture being driven by a positive MPS, a fracture surface similar to tensile and torsion specimens was expected. The detailed fracture surface analysis shown in Fig. 22 confirms the different steps in terms of successive crack surface patterns, and shows again that cracking initiates in the zone where the MPS is critical.

8 Conclusion and future work

The elastic, viscoplastic, and fracture behavior of the RTM6 epoxy resin was characterized as a function of strain rate and temperature under various loading conditions involving uniaxial tension, notched tension, uniaxial compression, torsion, and shear. When loaded in compression, RTM6 was shown to behave like amorphous thermoplastics in the glassy state, with the expected distinct deformation stages up to large strains, and exhibiting among others similar dependencies of the peak stress on temperature and strain-rates. Limited ductility was observed however for the other loading conditions. Unlike thermoplastics, brittle failure was always observed, and no progressive damage mechanism could be identified. Detailed fractographic analysis provided insight into the competition between shear yielding and maximum principal stress driven brittle failure.

A Drucker–Prager pressure-dependent constitutive model was built. A specific hardening law was developed with strain-rate and temperature dependent parameters, owing to Eyring’s theory of transition of state and to the theory of rubber elasticity. The pressure-dependence and hardening law, as well as four different failure criteria, were identified against the experimental results using a two-step procedure involving direct identification

and reverse analysis. This identification procedure requires at most four uniaxial compression tests and one uniaxial tensile test. After thorough verification, the constitutive model and a plastic strain at failure criterion were readily introduced in the standard version of Abaqus. The model was successfully assessed against results of progressive failure in V-notched beam shear test in terms of overall load–displacement curve, local shear-strain/shear-stress, and predicted failure path.

The present model is appropriate and has been validated for monotonic, radial or near radial loading. As a consequence, other approaches are pursued by the authors, in order to properly capture the unloading, fully reverse loading, creep, relaxation, and recovery behavior of RTM6, either based on phenomenological large strain constitutive models (e.g., Nguyen et al. 2015), or from physics-based micro-mechanical models (Morelle 2015). Though the pressure-dependent constitutive model and failure criteria provide satisfactory results in the range of stress-triaxialities addressed in this study, mainly through simple loading scenarios, they need further assessment against complex multi-axial loading conditions. Besides, perspectives involve the simulation of the deformation and failure of RTM-processed unidirectional composites loaded in transverse compression, using the constitutive model and failure criterion presented in the paper.

Acknowledgements The work was funded by the Fonds de la Recherche Scientifique through the FNRS doctoral fellowship of Xavier Morelle and the FRIA doctoral fellowship of Jérémie Chevalier. The authors are grateful to Maxime Melchior and Laurence Brassart for fruitful discussions and thank Alban Maton for his precious help with the machining of the numerous test samples.

References

- Ames, N.M., Srivastava, V., Chester, S.A., Anand, L.: A thermo-mechanically coupled theory for large deformations of amorphous polymers. Part II: applications. *Int. J. Plast.* **25**(8), 1495–1539 (2009). <http://linkinghub.elsevier.com/retrieve/pii/S074964190800171X>. doi:[10.1016/j.ijplas.2008.11.005](https://doi.org/10.1016/j.ijplas.2008.11.005)
- Anand, L., Gurtin, M.E.: A theory of amorphous solids undergoing large deformations, with application to polymeric glasses. *Int. J. Solids Struct.* **40**, 1465–1487 (2003)
- Anand, L., Ames, N.M., Srivastava, V., Chester, S.A.: A thermo-mechanically coupled theory for large deformations of amorphous polymers. Part I: formulation. *Int. J. Plast.* **25**(8), 1474–1494 (2009). <http://dx.doi.org/10.1016/j.ijplas.2008.11.004>
- Andrews, E.H., Reed, P.E.: Molecular fracture in polymers. In: Ferry, J. (ed.) *Failure in Polymers SE-1. Advances in Polymer Science*, vol. 27, pp. 1–66. Springer, Berlin (1978). http://dx.doi.org/10.1007/3-540-08829-6_1
- Argon, A.S.: A theory for the low-temperature plastic deformation of glassy polymers. *Philos. Mag.* **28**(4), 839–865 (1973). doi:[10.1080/14786437308220987](https://doi.org/10.1080/14786437308220987)
- Argon, A.S., Bessonov, M.I.: Plastic flow in glassy polymers. *Polym. Eng. Sci.* **17**(3), 174–182 (1977). <http://www.scopus.com/inward/record.url?eid=2-s2.0-0017466328&partnerID=ZOTx3y1>
- Arruda, E.M., Boyce, M.C.: A three-dimensional constitutive model for the large stretch behavior of rubber elastic materials. *J. Mech. Phys. Solids* **41**(2), 389–412 (1993). doi:[10.1016/0022-5096\(93\)90013-6](https://doi.org/10.1016/0022-5096(93)90013-6)
- Asp, L.E., Berglund, L.A., Talreja, R.: A criterion for crack initiation in glassy polymers subjected to a composite-like stress state. *Compos. Sci. Technol.* **56**(11), 1291–1301 (1996). doi:[10.1016/S0266-3538\(96\)00090-5](https://doi.org/10.1016/S0266-3538(96)00090-5)
- Bowden, P.B., Raha, S.: Molecular model for yield and flow in amorphous glassy polymers making use of a dislocation analogue (1974). <http://www.scopus.com/inward/record.url?eid=2-s2.0-0015995118&partnerID=ZOTx3y1>. doi:[10.1080/14786437408213560](https://doi.org/10.1080/14786437408213560)
- Boyce, M.C., Parks, D.M., Argon, A.S.: Large inelastic deformation of glassy polymers. Part I: rate dependent constitutive model. *Mech. Mater.* **7**(1), 15–33 (1988). doi:[10.1016/0167-6636\(88\)90003-8](https://doi.org/10.1016/0167-6636(88)90003-8)
- Canal, L.P., González, C., Segurado, J., LLorca, J.: Intraply fracture of fiber-reinforced composites: microscopic mechanisms and modeling. *Compos. Sci. Technol.* **72**(11), 1223–1232 (2012). doi:[10.1016/j.compscitech.2012.04.008](https://doi.org/10.1016/j.compscitech.2012.04.008)
- Cantwell, W., Roulin-Moloney, A., Kaiser, T.: Fractography of unfilled and particulate-filled epoxy resins. *J. Mater. Sci.* **23**, 1615–1631 (1988)

- Chevalier, J., Morelle, X., Bailly, C., Camanho, P., Pardoen, T., Lani, F.: Micro-mechanics based pressure dependent failure model for highly cross-linked epoxy resins. *Eng. Fract. Mech.* **158**, 1–12 (2016). <http://linkinghub.elsevier.com/retrieve/pii/S0013794416300571>. doi:[10.1016/j.engfracmech.2016.02.039](https://doi.org/10.1016/j.engfracmech.2016.02.039)
- Cohen, A.: A Padé approximant to the inverse Langevin function. *Rheol. Acta* **30**(3), 270–273 (1991). <http://dx.doi.org/10.1007/BF00366640>
- Drucker, D.: Limit analysis of two and three dimensional soil mechanics problems. *J. Mech. Phys. Solids* **1**(4), 217–226 (1953). doi:[10.1016/0022-5096\(53\)90001-5](https://doi.org/10.1016/0022-5096(53)90001-5)
- Drucker, D.C.: Plasticity theory, strength-differential (SD) phenomenon, and volume expansion in metals and plastics. *Metall. Trans. A, Phys. Metall. Mater. Sci.* **4**(March), 667–673 (1973)
- Dumont, D.: Thermoplastic as carrier for delivering carbon nanotubes and layered clay in epoxy resin for composite applications. Phd Thesis, Université catholique de Louvain (2013)
- Eyring, H.: Viscosity, plasticity, and diffusion as examples of absolute reaction rates. *J. Chem. Phys.* **4**(4), 283–291 (1936). <http://link.aip.org/link/JCPA6/v4/i4/p283/s1&Agg=doi>. doi:[10.1063/1.1749836](https://doi.org/10.1063/1.1749836)
- Fiedler, B., Hojo, M., Ochiai, S., Schulte, K., Ando, M.: Failure behavior of an epoxy matrix under different kinds of static loading. *Compos. Sci. Technol.* **61**(11), 1615–1624 (2001)
- Fiedler, B., Thomas, H., Schulte, K.: Influence of stress state and temperature on the strength of epoxy resins. In: 15th International Conference on Composites Materials, Durban, South Africa, p. 6376 (2005)
- Gearing, B.P., Anand, L.: On modeling the deformation and fracture response of glassy polymers due to shear-yielding and crazing. *Int. J. Solids Struct.* **41**(11–12), 3125–3150 (2004). doi:[10.1016/j.ijsolstr.2004.01.017](https://doi.org/10.1016/j.ijsolstr.2004.01.017)
- Gerlach, R., Sivior, C.R., Petrinic, N., Wiegand, J.: Experimental characterisation and constitutive modelling of RTM-6 resin under impact loading. *Polymer* **49**, 2728–2737 (2008). doi:[10.1016/j.polymer.2008.04.018](https://doi.org/10.1016/j.polymer.2008.04.018)
- Goldberg, R.K., Roberts, G.D., Gilat, A.: Incorporation of mean stress effects into the micromechanical analysis of the high strain rate response of polymer matrix composites. *Composites, Part B, Eng.* **34**, 151–165 (2003)
- Gómez-del Río, T., Rodríguez, J.: Compression yielding of epoxy: strain rate and temperature effect. *Mater. Des.* **35**, 369–373 (2012). <http://linkinghub.elsevier.com/retrieve/pii/S0261306911006595>. doi:[10.1016/j.matdes.2011.09.034](https://doi.org/10.1016/j.matdes.2011.09.034)
- Govaert, L.E., Timmermans, P.H.M., Brekelmans, W.A.M.: The influence of intrinsic strain softening on strain localization in polycarbonate: modeling and experimental validation. *J. Eng. Mater. Technol.* **122**(2), 177 (2000). doi:[10.1115/1.482784](https://doi.org/10.1115/1.482784)
- Govaert, L.E., Engels, T.A., Wendlandt, M., Tervoort, T.A., Suter, U.W.: Does the strain hardening modulus of glassy polymers scale with the flow stress? *J. Polym. Sci., Part B, Polym. Phys.* **46**, 2475–2481 (2008). <http://arxiv.org/abs/cond-mat/0406218>. doi:[10.1002/polb](https://doi.org/10.1002/polb)
- Greenhalgh, E.S., Hiley, M.J.: Fractography of polymer composites: current status and future issues. In: 13th European Conference on Composite Materials, Stockholm, Sweden (2008)
- G'Sell, C., Gómez, A.J.: Plastic banding in glassy polycarbonate under plane simple shear. *J. Mater. Sci.* **20**(10), 3462–3478. (1985). doi:[10.1007/BF01113753](https://doi.org/10.1007/BF01113753)
- G'Sell, C., Jonas, J.J.: Yield and transient effects during the plastic deformation of solid polymers. *J. Mater. Sci.* **16**(7), 1956–1974 (1981). doi:[10.1007/BF00540644](https://doi.org/10.1007/BF00540644)
- Hasan, O.A., Boyce, M.C.: A constitutive model for the nonlinear viscoelastic viscoplastic behavior of glassy polymers. *Polym. Eng. Sci.* **35**(4), 331 (1995)
- Hasan, O.A., Boyce, M.C., Li, X.S., Berko, S.: An investigation of the yield and postyield behavior and corresponding structure of poly (methyl methacrylate). *J. Polym. Sci., Part B, Polym. Phys.* **31**(2), 185–197 (1993). <http://www.scopus.com/inward/record.url?eid=2-s2.0-0027540142&partnerID=ZOtx3y1>. doi:[10.1002/polb.1993.090310207](https://doi.org/10.1002/polb.1993.090310207)
- Haward, R., Bowden, P.: The Physics of Glassy Polymers. *Appl. Sci., Braking* (1973). Chap. 5
- Haward, R., Thackray, G.: *Proc. R. Soc.* **302**, 453 (1968)
- Hobbiebrunken, T., Fiedler, B.: Experimental determination of the true epoxy resin strength using micro-scaled specimens. *Composites, Part A, Appl. Sci. Manuf.* **38**, 814–818 (2007). doi:[10.1016/j.compositesa.2006.08.006](https://doi.org/10.1016/j.compositesa.2006.08.006)
- Hobbiebrunken, T., Fiedler, B., Hojo, M., Ochiai, S., Schulte, K.: Microscopic yielding of CF/epoxy composites and the effect on the formation of thermal residual stresses. *Compos. Sci. Technol.* **65**, 1626–1635 (2005). doi:[10.1016/j.compscitech.2005.02.003](https://doi.org/10.1016/j.compscitech.2005.02.003)
- Hodgkinson, J.: Mechanical Testing of Advanced Fibre Composites. Woodhead, Cambridge (2000). CRC Press LLC
- Homer, E.R., Schuh, C.A.: Mesoscale modeling of amorphous metals by shear transformation zone dynamics. *Acta Mater.* **57**(9), 2823–2833 (2009). <http://dx.doi.org/10.1016/j.actamat.2009.02.035>. doi:[10.1016/j.actamat.2009.02.035](https://doi.org/10.1016/j.actamat.2009.02.035)

- Jatin, Sudarkodi, V., Basu, S.: Investigations into the origins of plastic flow and strain hardening in amorphous glassy polymers. *Int. J. Plast.* **56**, 139–155 (2013). <http://dx.doi.org/10.1016/j.ijplas.2013.11.007>
- Kausch, H., Heymans, N., Plummer, C.J., Decroly, P.: *Traité des Matériaux: Matériaux Polymères—Propriétés Mécaniques et Physiques*. Presse Polytechniques et Universitaires Romandes, Lausanne (2001)
- Kinloch, A., Young, R.: *Fracture Behaviour of Polymers*. Springer, Netherlands (1983)
- Kiuna, N., Lawrence, C.J., Fontana, Q.P.V., Lee, P.D., Selerland, T., Spelt, P.D.M.: A model for resin viscosity during cure in the resin transfer moulding process. *Composites, Part A, Appl. Sci. Manuf.* **33**(11), 1497–1503 (2002). doi:10.1016/S1359-835X(02)00177-X
- Klompen, E.T.J., Govaert, L.E.: Nonlinear viscoelastic behaviour of thermorheologically complex materials. *Mech. Time-Depend. Mater.* **3**(1), 49–69 (1999). doi:10.1023/A:1009853024441
- Klompen, E.T.J., Engels, T.A.P., Govaert, L.E., Meijer, H.E.H.: Modeling of the postyield response of glassy polymers: influence of thermomechanical history. *Macromolecules* **38**(16), 6997–7008 (2005)
- Liang, Y.M., Liechti, K.M.: On the large deformation and localization behavior of an epoxy resin under multi-axial stress states. *Int. J. Solids Struct.* **33**(10), 1479–1500 (1996). doi:10.1016/0020-7683(95)00105-0
- LLorca, J., González, C., Molina-Aldareguía, J.M., Segurado, J., Seltzer, R., Sket, F., Rodríguez, M., Sádaba, S., Muñoz, R., Canal, L.P.: Multiscale modeling of composite materials: a roadmap towards virtual testing. *Adv. Mater.* **23**(44), 5130–5147 (2011). <http://doi.wiley.com/10.1002/adma.201101683>
- Manjoine, M.: Multiaxial Stress and Fracture. In: Liebowitz, H. (ed.): pp. 265–309. Academic Press, London (1971)
- Marano, C., Rink, M.: Viscoelasticity and shear yielding onset in amorphous glassy polymers. *Mech. Time-Depend. Mater.* **10**(3), 173–184 (2006). <http://www.springerlink.com/index/10.1007/s11043-006-9016-z>
- Marano, C., Rink, M.: Effect of loading history and material's structural state on the yield onset of a poly-methylmethacrylate. *Mech. Time-Depend. Mater.* **13**(1), 37–48 (2008). <http://www.springerlink.com/index/10.1007/s11043-008-9072-7>
- Meijer, H.E., Govaert, L.E.: Mechanical performance of polymer systems: the relation between structure and properties. *Prog. Polym. Sci.* **30**(8–9), 915–938. (2005). <http://linkinghub.elsevier.com/retrieve/pii/S007967005000717>
- Melick, H.G.H.V., Govaert, L.E., Meijer, H.E.H.: Localisation phenomena in glassy polymers: influence of thermal and mechanical history. *Polymer* **44**, 3579–3591 (2003a). doi:10.1016/S0032-3861(03)00089-2
- Melick, H.G.H.V., Govaert, L.E., Meijer, H.E.H.: On the origin of strain hardening in glassy polymers. *Polymer* **44**, 2493–2502 (2003b). doi:10.1016/S0032-3861(03)00112-5
- Morelle, X.P.: Mechanics and Micro-mechanisms of a Highly-Crosslinked Epoxy Resin. Phd Thesis, Université catholique de Louvain (2015)
- Morelle, X.P., Bahrami, A., Lani, F., Melchior, M.A., Nysten, B., Bailly, C., Pardoën, T.: Characterization and modeling of the time-dependent behavior of the RTM6 structural epoxy involving recovery, creep and back stress. In: 16th European Conference on Composite Materials, Sevilla, Spain (2014)
- Morgan, R.J., Mones, E.T., Steele, W.J.: Tensile deformation and failure processes of amine-cured epoxies. *Polymer* **23**(2), 295–305 (1982). <http://www.sciencedirect.com/science/article/B6TXW-48CWBY5-5R/2/0ea67cbfef1536b711aaa71eadf944a5>
- Narisawa, I., Murayama, T., Ogawa, H.: Internal fracture of notched epoxy resins. *Polymer* **23**(2), 291–294 (1982). <http://www.sciencedirect.com/science/article/pii/0032386182903196>
- Nguyen, V., Morelle, X., Lani, F., Pardoën, T., Bailly, C., Noels, L.: A viscoelastic–viscoplastic-damage constitutive model based on a large strain hyperelastic formulation for amorphous glassy polymers. In: 20th International Conference on Composite Materials, Copenhagen, Denmark (2015)
- Oleynik, E.: Plastic deformation and mobility in glassy polymers. *Prog. Colloid & Polym. Sci.* **80**, 140–150 (1989). <http://dx.doi.org/10.1007/BFb0115425>
- Poulain, X., Kohlman, L.W., Binienda, W., Roberts, G.D., Goldberg, R.K., Benzerga, A.A.: Determination of the intrinsic behavior of polymers using digital image correlation combined with video-monitored testing. *Int. J. Solids Struct.* **50**(11–12), 1869–1878 (2013). <http://dx.doi.org/10.1016/j.ijsolstr.2013.01.041>
- Poulain, X., Benzerga, A.A., Goldberg, R.K.: Finite-strain elasto-viscoplastic behavior of an epoxy resin: experiments and modeling in the glassy regime. *Int. J. Plast.* **62**, 138–161. (2014). <http://www.sciencedirect.com/science/article/pii/S0749641914001351>
- Quinson, R., Perez, J., Rink, M., Pavon, A.: Components of non-elastic deformation in amorphous glassy polymers. *J. Mater. Sci.* **31**, 4387–4394 (1996)
- R2015 M (2015)
- Ree, T., Eyring, H.: Theory of non-Newtonian flow. I. Solid plastic system. *J. Appl. Phys.* **26**(7), 793–800 (1955). doi:10.1063/1.1722098

- Rottler, J.: Fracture in glassy polymers: a molecular modelling perspective. *J. Polym. Sci., Part B, Polym. Phys.* 1–19 (2009). doi:[10.1088/0953-8984/21/46/463101](https://doi.org/10.1088/0953-8984/21/46/463101)
- Roulin-Moloney, A.: Fractography and Failure Mechanics of Polymers and Composites. Elsevier Appl. Sci., London (1989)
- Senden, D., Van Dommelen, J., Govaert, L.E.: Strain hardening and its relation to bauschinger effects in oriented polymers. *J. Polym. Sci., Part B, Polym. Phys.* **48**, 1483–1494 (2010). doi:[10.1002/POLB](https://doi.org/10.1002/POLB)
- Sindt, O., Perez, J., Gerard, J.F.: Molecular architecture-mechanical behaviour relationships in epoxy networks. *Polymer* **37**(14), 2989–2997 (1996). doi:[10.1016/0032-3861\(96\)89396-7](https://doi.org/10.1016/0032-3861(96)89396-7)
- Srivastava, V., Chester, S.A., Ames, N.M., Anand, L.: A thermo-mechanically-coupled large-deformation theory for amorphous polymers in a temperature range which spans their glass transition. *Int. J. Plast.* **26**(8), 1138–1182 (2010). <http://linkinghub.elsevier.com/retrieve/pii/S0749641910000057>. doi:[10.1016/j.ijplas.2010.01.004](https://doi.org/10.1016/j.ijplas.2010.01.004)
- Struik, L.C.E.: Some problems in the non-linear viscoelasticity of amorphous glassy polymers. *J. Non-Cryst. Solids* **133**, 395–407 (1991)
- Tervoort, T., Klompen, E.J., Govaert, L.E.: A multi-mode approach to finite, three-dimensional, nonlinear viscoelastic behavior of polymer glasses. *J. Rheol.* **40**(5), 779 (1996). doi:[10.1122/1.550755](https://doi.org/10.1122/1.550755)
- Tervoort, T.A., Govaert, L.E.: A constitutive equation for the elasto-viscoplastic deformation of glassy polymers. *Mech. Time-Depend. Mater.* **1**, 269–291 (1998)
- V6.12 A (2016)
- Westbrook, K.K., Kao, P.H., Castro, F., Ding, Y., Jerry Qi, H.: A 3D finite deformation constitutive model for amorphous shape memory polymers: a multi-branch modeling approach for nonequilibrium relaxation processes. *Mech. Mater.* **43**(12), 853–869 (2011). <http://linkinghub.elsevier.com/retrieve/pii/S0167663611001761>. doi:[10.1016/j.mechmat.2011.09.004](https://doi.org/10.1016/j.mechmat.2011.09.004)
- Wu, P., van der Giessen, E.: On neck propagation in amorphous glassy polymers under plane strain tension. *Int. J. Plast.* **11**(3), 211–235 (1995). doi:[10.1016/0749-6419\(94\)00043-3](https://doi.org/10.1016/0749-6419(94)00043-3)
- Wu, P., van der Giessen, E.: On improved network models for rubber elasticity and their applications to orientation hardening in glassy polymers. *J. Mech. Phys. Solids* **41**(3), 427–456 (1993). doi:[10.1016/0022-5096\(93\)90043-F](https://doi.org/10.1016/0022-5096(93)90043-F)
- Yamini, S., Young, R.J.: The mechanical properties of epoxy resins—Part 1: mechanisms of plastic deformation. *J. Mater. Sci.* **15**(7), 1814–1822 (1980). doi:[10.1007/BF00550603](https://doi.org/10.1007/BF00550603)